Easy snap-folding of hexagonal ring origami by geometric modifications

Lu Lu [a,1], Sophie Leanza [a,1], Jize Dai [a,1], Xiaohao Sun [b], Ruike Renee Zhao [a,*]

[a] *Department of Mechanical Engineering, Stanford University, Stanford, CA 94305, USA*
[b] *The George W. Woodruff School of Mechanical Engineering, Georgia Institute of Technology, Atlanta, GA 30332, USA*

ARTICLE INFO

ABSTRACT

Hexagonal ring origami is a type of foldable structure that has impressive packing abilities and can be tessellated into two-dimensional or three-dimensional surfaces without any gap or overlap. It can be folded under bending or twisting loads into a peach core-shaped configuration with only 10.6% of its initial area. However, in applications of large-scale foldable structures, folding by bending or twisting is usually technically difficult. Here, we propose strategies to facilitate easy snap-folding of the hexagonal ring by a simple point load or localized twist or squeeze. This is enabled by two geometric modifications made to the hexagonal ring: introducing residual strain and creating pre-twisted edges. By combining theoretical modeling, finite element simulations, and experiments, we systematically investigate the snap-folding behaviors of modified hexagonal rings with residual strain and pre-twisted edges. It is found that the geometric modifications promote easy snap-folding of the hexagonal ring by different mechanisms: introducing residual strain can significantly decrease the energy barrier and thus reduce the required moment to snap-fold the ring, while creating pre-twisted edges allows for easy out-of-plane deformation which is a necessary condition for a ring to fold. Combining the two methods further enables the snap-folding of the hexagonal ring by a point load or localized twist or squeeze. To demonstrate the easy folding of large assemblies of the modified rings, we construct various structures that can be snap-folded from their initial three-dimensional states to significantly lower-volume final states by a simple compression at the corners of the rings. We envision that the proposed geometric modification strategies can provide a new perspective on the rational design of easy-to-fold ring origami-based foldable functional structures with extremely high packing ratios.

1. Introduction

Ring origami is a class of foldable structures having closed-loop configurations with different geometries, such as two-dimensional (2D) rings with different shapes, three-dimensional (3D) ring trusses, toroidal tubes, and any ring-like geometries (Gan and Pellegrino, 2006; Ishida et al., 2015; Mouthuy et al., 2012; Sharma and Upadhyay, 2022; Wu et al., 2021; You and Pellegrino, 1997). Ring origami provides effective strategies to design deployable and reconfigurable functional structures with impressive packing abilities. Pertinent examples of functional reconfigurable structures include emergency shelters (Melancon et al., 2021), stadium covers (Filipov et al.,
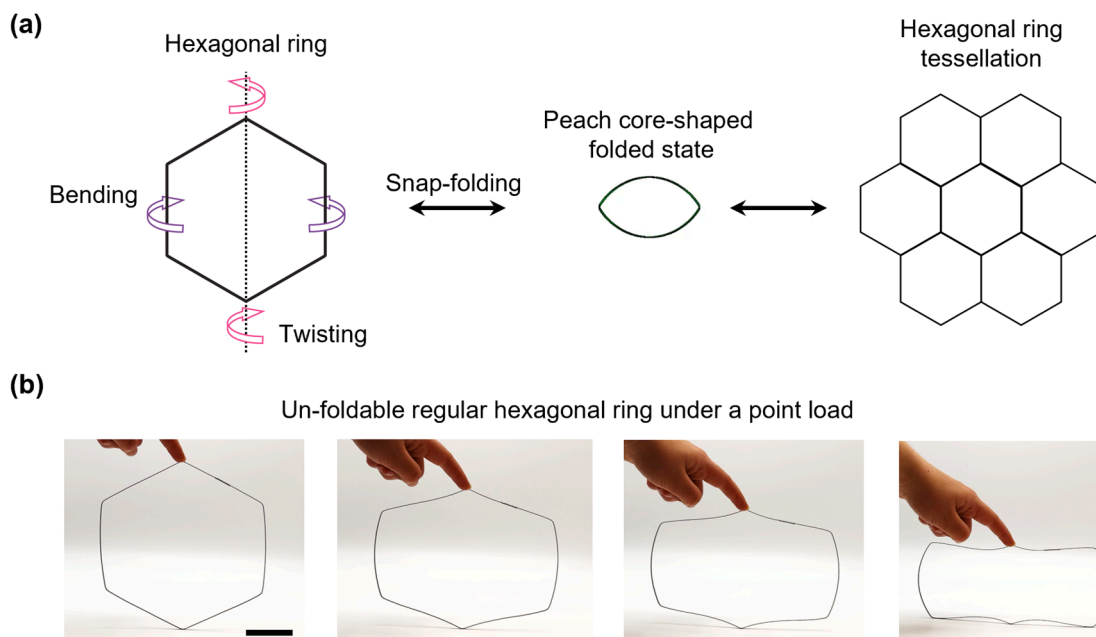

Fig. 1. Folding of regular hexagonal ring and its tessellation. (a) Snap-folding of a regular hexagonal ring under a pair of bending or twisting loads and a foldable hexagonal ring tessellation. (b) Deformation process of an un-foldable regular hexagonal ring under a point load. Scale bar: 50 mm.

2015), solar panels (Chen et al., 2019; Zirbel et al., 2013), flexible electronics (Fu et al., 2018; Luan et al., 2021; Yan et al., 2022; Zhang et al., 2021), medical stents (Kuribayashi et al., 2006; Zhao et al., 2012), deployable antennas (Han et al., 2019; Santiago-Prowald and Baier, 2013), and space habitats (Cadogan et al., 1999; Chen et al., 2021). Among different ring origami systems, there is a type of ring formed by closed-loop rods that can snap-fold, triggered by the mechanical instability of the rod under external loads. It has been shown that the ring with rationally designed geometric parameters can fold, in a self-guided manner, to a small-volume configuration by harnessing the snap-through instability induced by either bending or twisting loads (Sun et al., 2022a; Wu et al., 2021; Yoshiaki et al., 1992). Among various types of rings, the hexagonal ring exhibits promising functional features including its high packing ratio from deployed to folded state and its ability to form gapless 2D and 3D tessellations (Leanza et al., 2022; Wu et al., 2022). These features make the hexagonal ring an ideal candidate to serve as building blocks of large foldable structures in engineering applications. As shown in Fig. 1(a), when subjected to a pair of sufficiently large bending or twisting loads, the hexagonal ring can be snap-folded into three overlapping loops with a peach core-shaped configuration that is only 10.6% of the initial area. Further, the packing ratio can be even more significant when folding assemblies of rings, such as a planar tessellation of multiple hexagonal rings (Fig. 1(a)).

However, in applications where hexagonal rings are assembled into large-scale foldable structures, it is usually technically difficult to fold the whole structure, mainly due to two reasons: (i) to fold a single ring, it always requires two loading points to initiate either bending or twisting deformation; (ii) the required moment is relatively large. To enhance the feasibility and versatility of hexagonal ring-based large-scale functional structures, hexagonal rings that facilitate easy folding upon a much-reduced load magnitude and simplified loading method, such as localized loading through a point load, are desired. Motivated by this goal, geometric modifications of the regular hexagonal ring are explored in this work for easy snap-folding of the hexagonal ring. A regular hexagonal ring is formed by reshaping a straight steel ribbon to the hexagonal shape. Fig. 1(b) shows the deformation process of a regular ring under a point load, during which the ring only exhibits in-plane contraction and does not fold (see Movie 1 in Supplementary Materials for details). Since the hexagonal ring requires out-of-plane deformation to fold and its internal energy needs to overcome a certain energy barrier to trigger snapping, ring systems with rational design that promote both conditions could potentially lead to easy folding with low required load and simple loading methods. Here, we explore the easy folding of rings by making design modifications, namely by introducing residual strain and pre-twisted edges (see Fig. 2(a)). The residual strain provides internal strain energy, which can favor easy snapping. The pre-twisted edges are created by twisting the two ends of each straight edge, which can break the symmetry of the hexagonal ring and induce out-of-plane deformation when under a point load. As demonstrated in experimental implementations in Fig. 2(b) and (c), the modified hexagonal ring with residual strain and slightly pre-twisted edges (around 5° at both ends of each edge) can easily snap-fold to the peach core shape under a point load or a localized twist at one corner (see Movies 1 and 2 in Supplementary Materials for details and additional easy folding methods). The modification of the hexagonal ring opens the way to design easy-to-fold 2D or 3D functional structures by assembling the rings, such as the orthogonally assembled rings, which fold under a point load as shown in Fig. 2(d) (see Movie 1 in Supplementary Materials). Motivated by this finding, the present work aims to provide theoretical understanding of the influences of residual strain and pre-twisted edges on the snap-folding behaviors of hexagonal rings, and thus guide the rational design of easy-to-fold ring origami-based functional structures with high packing ratio.

Instabilities of slender structures (such as rods, rings, strips, and ribbons) have been intensively studied during the past decades due
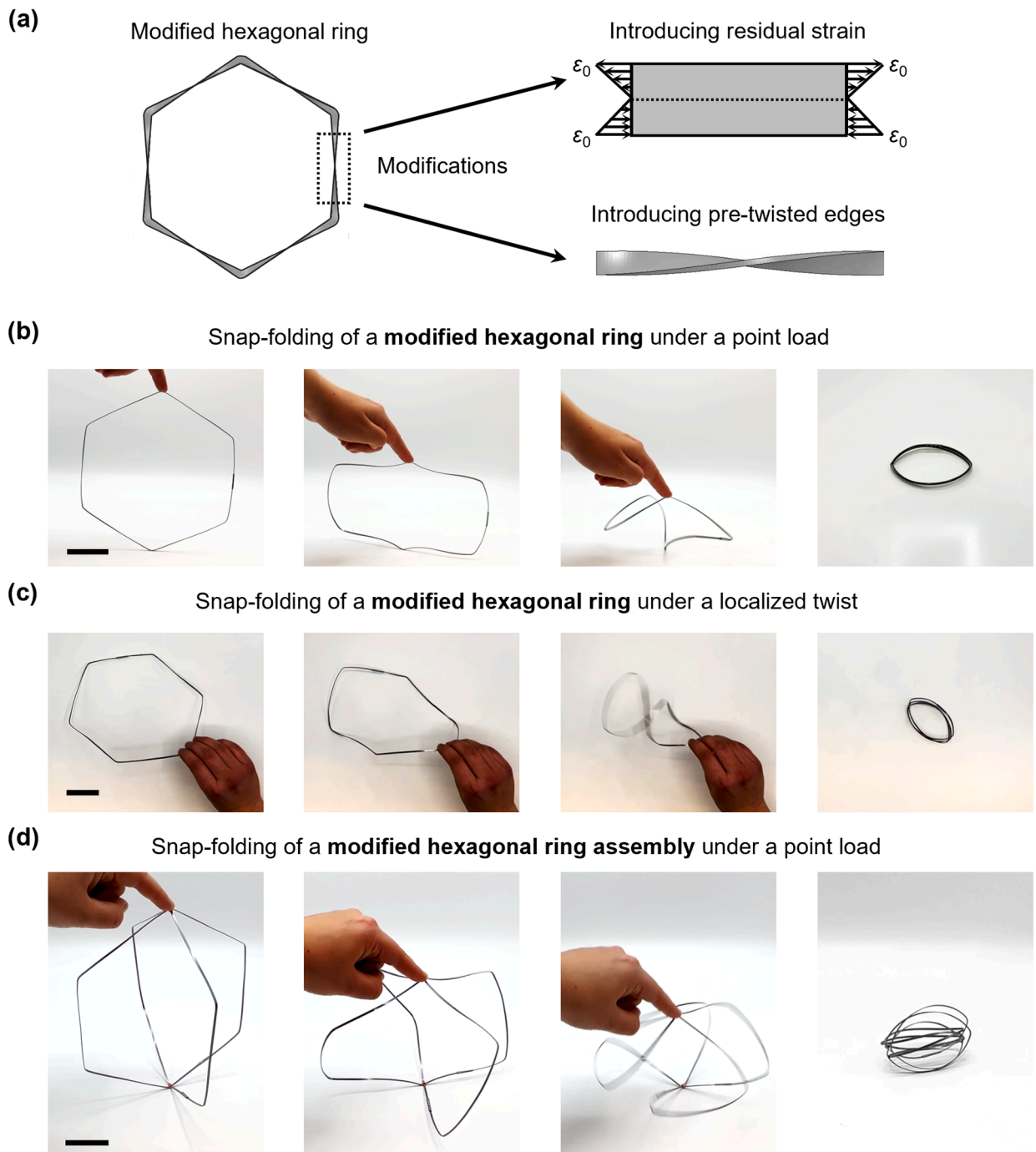
(a)

(b)

Snap-folding of a **modified hexagonal ring** under a point load

(c)

Snap-folding of a **modified hexagonal ring** under a localized twist

(d)

Snap-folding of a **modified hexagonal ring assembly** under a point load

Fig. 2. Snap-folding of modified hexagonal ring and its assembly. (a) Geometric modifications of hexagonal ring by introducing residual strain and pre-twisted edges. (b,c) Snap-folding of a modified hexagonal ring under a point load (b), or a localized twist at one corner (c). (d) Snap-folding of orthogonally assembled modified hexagonal rings under a point load. Scale bars: 50 mm.

to their rich nonlinear structural behaviors and widespread applications. Diverse examples can be found in nature and engineering applications, such as growth-induced instabilities of biological filaments (Kaczmarski et al., 2022; Lessinnes et al., 2017;Moulton et al., 2013; Moulton et al., 2020), swelling induced-instabilities of embedded cylindrical inclusions (Hutchinson, 2020), bending instability of rod-shaped bacteria (Qiu et al., 2022), buckling of hard-magnetic rods (Barreto et al., 2022; Sano et al., 2022), curvature-induced instability of curved origami (Dias and Audoly, 2014; Dias et al., 2012), bifurcations of bigon rings (Yu et al., 2021) and pre-buckled bands (Huang et al., 2020; Yu and Hanna, 2019), and snap-instabilities of constraint strips (Gomez et al., 2017; Liu et al., 2021; Sano and Wada, 2019). In addition to understanding these fantastic phenomena, researchers have also focused on the instabilities of twisted slender structures (Audoly and Neukirch, 2021; Coleman and Swigon, 2004; Dinh et al., 2016; Domokos and Healey, 2001; Goriely, 2006; Korte et al., 2011; Manning and Maddocks, 1999; Neukirch et al., 2002). By using the twisted slender structures, some novel phenomena and applications have been uncovered. For example, a twisted ribbon under tension can trigger diverse instability modes by simply controlling the tension and the twist angle, ranging from helicoid, buckled helicoid, and creased helicoid to localized loop (Chopin and Kudrolli, 2013). Pre-twisted ribbons can serve as compliant joints to create shape-morphing structures due to their preferred bending directions along the lengths (Celli et al., 2020). Residual stress is another factor that can significantly affect the instabilities of slender structures. One typical example is the overcurved ring (Mouthuy et al., 2012), in which the residual stress triggers the buckling of an initial planar ring to a saddle shape. Another example includes growing filamentary structures (Moulton et al., 2020), in which the growth-induced residual stress can alter both the stiffness and the intrinsic curvature of the filament. Although there have been some studies on rings with residual stress or pre-twist (Domokos and Healey, 2001; Goriely, 2006; Manning and Maddocks, 1999;Moulton et al., 2013; Mouthuy et al., 2012), they are only limited to the instabilities of circular rings.

To fully take advantage of the hexagonal ring's large packing ratio and its tessellation capability for large foldable structures, we explore how geometric modifications, i.e., introducing residual strain and pre-twisted edge, can be utilized to achieve the easy folding of hexagonal rings. In this work, we combine experiments, finite element simulations, and theoretical modeling to systematically study the snap-folding behaviors of modified hexagonal rings with residual strain and pre-twisted edges. In experiments, the modified hexagonal ring is fabricated by manually reshaping a stress-free regular stainless steel hexagonal ring. The residual strain induced in the ring is simulated by considering a bilayer hexagonal ring whose inner layer is under thermal contraction while the outer layer is under thermal expansion. Kirchhoff rod theory is used to model the rings. Our theoretical, numerical, and experimental results show that both introducing residual strain and pre-twisted edges can facilitate the easy snap-folding of the ring. More interestingly, we find that the coupling of residual strain and pre-twisted edges enables the snap-folding of the modified hexagonal ring under a point load. The present work provides new design strategies for easy folding of ring origami-based structures, which have broad applications in the fields of space structures, architecture engineering, and biomedical devices.

The paper is organized as follows. In Section 2, we introduce the fabrication of the hexagonal ring with residual strain, and use finite element analysis (FEA) and theoretical modeling to study the effect of residual strain on the snap-folding behavior of the modified hexagonal ring. In Section 3, we investigate the influence of pre-twisted edges and its coupling with residual strain on the snap-folding behavior of the modified hexagonal ring. In Section 4, we present two assemblies of the modified hexagonal rings which can be snap-folded under a point load. In Section 5, we conclude the main findings of this work.

2. Modified hexagonal ring with residual strain

In this section, we investigate how residual strain affects the snap-folding and stability of the hexagonal ring under either twisting or bending loads. We start from introducing the fabrication of a modified hexagonal ring with residual strain. FEA simulations and theoretical modeling are then conducted to study the snap-folding behavior of the modified hexagonal ring. Finally, we perform a parametric study on residual strain magnitude, loading position, and loading method to qualitatively and quantitatively discuss the effect of residual strain on the snap-folding behavior of the modified hexagonal ring.

2.1. Fabrication of the hexagonal ring with residual strain

As shown in Fig. 3(a), our hexagonal ring is fabricated by manually reshaping a regular stress-free stainless steel hexagonal ring, which has edge length $a = 100$ mm and corner radius $r = 5$ mm. The ring has a rectangular cross-section with height $h = 2$ mm and thickness $t = 0.5$ mm. We first disconnect the stress-free hexagonal ring and plastically deform the ring by winding it inward to obtain the natural state of the modified ring. Different natural states can be achieved by controlling the plastic deformation in the ring. Then, we reconnect the ring back to the hexagonal shape by applying bending moments to the two ends to unwind it (see Movie 3 in Supplementary Materials). In this way, the residual strain equivalent to an internal moment is introduced in the ring. Note that the residual strain is elastic, as no plastic deformation is induced during the reconnection of the ring.

2.2. Finite element simulations

Next, we study the snap-folding behavior of the modified hexagonal ring with residual strain using FEA simulations. To account for the residual strain, we consider a disconnected bilayer hexagonal ring with the same geometric parameters as the fabricated ring, as shown in Fig. 3(b). The two layers are perfectly bounded and have the identical Young's moduli E. The coefficients of thermal expansion (CTE) in the two layers are equal in magnitude but opposite in sign. In particular, the inner layer has a negative CTE $-\alpha_\text{T}$, while the outer layer has a positive α_T, such that the inner layer tends to shrink while the outer layer tends to expand when subjected to a temperature rise ΔT. As a result, the strain mismatch between the two layers triggers the disconnected ring to deform by winding

(a)

Natural states of the modified hexagonal ring (experiment)

(b)

Induce ring deformation through thermal strain (ε_T)

(c)

Natural states of the modified hexagonal ring (FEA)
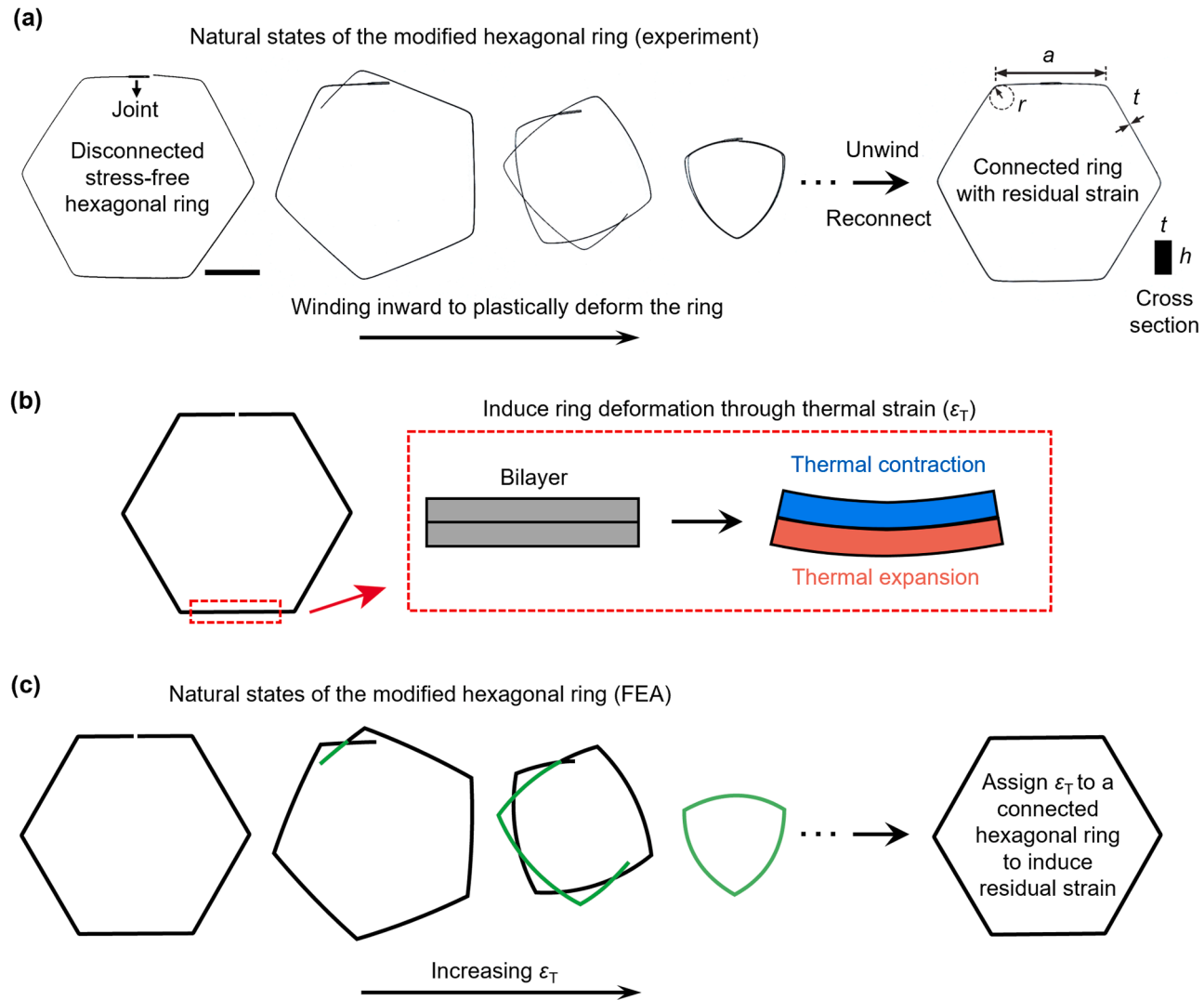
Increasing ε_T

Fig. 3. Fabrication and FEA simulation strategies of the modified hexagonal ring with residual strain. (a) Fabrication process of the modified hexagonal ring with controlled residual strain. Scale bar: 50 mm. (b) A disconnected bilayer ring considered in FEA simulations, whose inner layer is under thermal contraction and outer layer is under thermal expansion. (c) Natural states of the disconnected hexagonal ring in FEA simulations driven by increasing the thermal strain.

inward. By increasing the thermal strain ε_T ($=\alpha_T \Delta T$), we obtain a series of multi-loop configurations (see Fig. 3(c) and Movie 3 in Supplementary Materials). Once the deformed bilayer hexagonal ring reaches the same configuration as the natural state of the disconnected ring in the experiment, the corresponding thermal strain can be assigned to an initially stress-free connected hexagonal ring in the simulation to replicate the residual strain in the fabricated hexagonal ring. The snap-folding behavior of the ring is then simulated by applying bending or twisting loads. In the simulation, the Young's modulus is taken as $E = 200$ GPa, Poisson's ratio is 0.3, and the CTE is set as $\alpha_T = 0.002$ K^{-1}.

2.3. Theoretical modeling

To understand the underlying mechanism of how residual strain affects the snap-folding of the modified hexagonal ring, we employ the Kirchhoff rod theory to model the modified hexagonal ring and then compare the results with the FEA simulations, which are further validated by experiments. The geometry of the hexagonal ring with rectangular cross-section is defined in Fig. 4(a), in which a and r represent the edge length and the corner radius, respectively, and h and t denote the height and the thickness of the cross-section, respectively. To quantify the residual strain introduced in the experiment, a Cartesian coordinate system (x, y, z) is established at the centerline of the ring's bottom edge, in which x and y axes are aligned with the thickness and longitudinal directions of the edge, respectively, and the z axis is along the height direction (pointing out of the plane). Since only a small deformation is induced in the ring during the reconnection of the ring by bending, the residual strain is elastic (validated by reversible configurations of the connected and disconnected ring in Movie 3 in Supplementary Materials) and linearly distributed along the thickness, as shown in Fig. 4 (b). Here, we define ε_0 as the maximum residual strain, which is on the surface of the ring. Details on determination of the residual strain in a ring with a specific natural state are provided in Appendix A.

Kirchhoff rod model is the most commonly used theoretical tool to study the mechanical behaviors of slender structures (Audoly and Pomeau, 2010; Dill, 1992; Grandgeorge et al., 2022; Miller et al., 2014;Moulton et al., 2013; Patil et al., 2020; Starostin and Van Der Heijden, 2007). Here, we adopt the Kirchhoff rod model while making necessary modifications such that it can capture the effect of residual strain introduced in our hexagonal ring. Consider a naturally curved inextensible and unshearable rod shown in Fig. 4(c). The centerline of the rod is parameterized by a position vector $\mathbf{r}(s)$ in the global orthonormal basis ($\mathbf{E}_1$, $\mathbf{E}_2$, $\mathbf{E}_3$), where $s \in [0, L]$ is the arc length and L is the total length of the rod. Due to the inextensible assumption, L remains unchanged during the deformation. Moreover, a local orthonormal basis [$\mathbf{e}_1(s)$, $\mathbf{e}_2(s)$, $\mathbf{e}_3(s)$] obeying the right-hand convention (i.e., $\mathbf{e}_1 \times \mathbf{e}_2 = \mathbf{e}_3$) is attached to the centerline, in which $\mathbf{e}_1(s)$ and $\mathbf{e}_2(s)$ are two unit vectors along the height and the thickness directions of the rod, and $\mathbf{e}_3(s)$ is a unit vector along the tangent direction of the centerline. By introducing the local basis, the kinematic equations of the rod can be obtained as

$$\mathbf{e}_3(s) = \frac{d\mathbf{r}(s)}{ds}, \tag{1}$$

$$\frac{d\mathbf{e}_i(s)}{ds} = \boldsymbol{\omega}(s) \times \mathbf{e}_i(s), i = 1, 2, 3, \tag{2}$$

in which $\boldsymbol{\omega}(s) = \kappa_1(s)\mathbf{e}_1(s) + \kappa_2(s)\mathbf{e}_2(s) + \kappa_3(s)\mathbf{e}_3(s)$ is the Darboux vector with $\kappa_1(s)$ and $\kappa_2(s)$ being the bending curvatures, and $\kappa_3(s)$ being the twisting curvature.

The stress acting on the cross-section of the rod at $\mathbf{r}(s)$ produces a resultant force $\mathbf{F}(s)$ and a resultant moment $\mathbf{M}(s)$ attached to the centerline. According to the Kirchhoff rod theory, the balance of linear and angular momenta associated with $\mathbf{F}(s)$ and $\mathbf{M}(s)$ gives

$$\frac{d\mathbf{F}(s)}{ds} + \mathbf{f}(s) = \mathbf{0}, \frac{d\mathbf{M}(s)}{ds} + \frac{d\mathbf{r}(s)}{ds} \times \mathbf{F}(s) + \mathbf{m}(s) = \mathbf{0}, \tag{3}$$

where $\mathbf{f}(s)$ and $\mathbf{m}(s)$ are the body force and couple per unit length, such as gravity, viscous force, or interaction force between different parts of the rod. In the present work, there is no body force or couple, i.e., $\mathbf{f}(s) = 0$ and $\mathbf{m}(s) = 0$. With the consideration of the resultant moment M_R of the residual stress in Eq. (A.5), $\mathbf{F}(s)$ and $\mathbf{M}(s)$ are given by

$$\mathbf{F}(s) = F_1(s)\mathbf{e}_1(s) + F_2(s)\mathbf{e}_2(s) + F_3(s)\mathbf{e}_3(s), \tag{4}$$

$$\mathbf{M}(s) = [M_1(s) + M_R]\mathbf{e}_1(s) + M_2(s)\mathbf{e}_2(s) + M_3(s)\mathbf{e}_3(s), \tag{5}$$

in which $F_i(s)$ and $M_i(s)$ ($i = 1, 2, 3$) are the components of $\mathbf{F}(s)$ and $\mathbf{M}(s)$. Then, the linear constitutive relations for the moments are considered, which are written as

$$\mathbf{M}(s) = \{EI_1[\kappa_1(s) - \kappa_{01}(s)] + M_R\}\mathbf{e}_1(s) + EI_2[\kappa_2(s) - \kappa_{02}(s)]\mathbf{e}_2(s) + GJ[\kappa_3(s) - \kappa_{03}(s)]\mathbf{e}_3(s). \tag{6}$$

Here, $\kappa_{01}(s)$, $\kappa_{02}(s)$, and $\kappa_{03}(s)$ are the two bending curvatures and the twisting curvature in the initial configuration, which also defines the natural state of the rod. E represents the Young's modulus of the rod, and $G = E/[2(1+\nu)]$ denotes the shear modulus with ν being the Poisson's ratio. I_1 and I_2 are the moments of inertia with respect to the height direction and thickness direction, respectively, and J is the rotational constant. For the hexagonal ring with rectangular cross section, these quantities are given by Timoshenko and Goodier (1951)
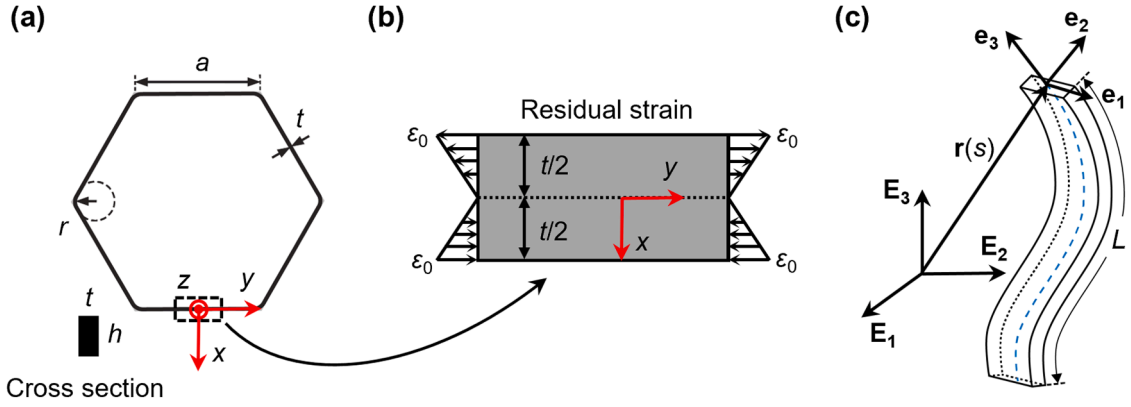
Fig. 4. Schematics of the hexagonal ring and the rod model. (a) Geometric parameters of the hexagonal ring. (b) Distribution of the residual strain along the thickness of the hexagonal ring in the theoretical model. (c) Local basis (e_1, e_2, e_3) and global basis (E_1, E_2, E_3) of the Kirchhoff rod model.

$$I_1 = \frac{ht^3}{12}, I_2 = \frac{h^3 t}{12}, J = \frac{ht^3}{3}\left\{1 - \frac{192}{\pi^5}\frac{t}{h}\sum_{n=1}^{\infty}\frac{1}{(2n-1)^5}\tanh\left[\frac{(2n-1)\pi h}{2t}\right]\right\}. \tag{7}$$

Note that there are no constitutive relations for the resultant force $\mathbf{F}(s)$ since the rod is assumed to be inextensible and unshearable. By projecting Eq. (3) along the local basis [$e_1(s)$, $e_2(s)$, $e_3(s)$] and using Eq. (6), one can obtain six equilibrium equations as follows:

$$\frac{dF_1}{ds} - F_2\kappa_3 + F_3\kappa_2 = 0, \tag{8}$$

$$\frac{dF_2}{ds} - F_3\kappa_1 + F_1\kappa_3 = 0, \tag{9}$$

$$\frac{dF_3}{ds} - F_1\kappa_2 + F_2\kappa_1 = 0, \tag{10}$$

$$EI_1\left(\frac{d\kappa_1}{ds} - \frac{d\kappa_{01}}{ds}\right) - EI_2(\kappa_2 - \kappa_{02})\kappa_3 + GJ(\kappa_3 - \kappa_{03})\kappa_2 - F_2 = 0, \tag{11}$$

$$EI_2\left(\frac{d\kappa_2}{ds} - \frac{d\kappa_{02}}{ds}\right) + [EI_1(\kappa_1 - \kappa_{01}) + M_R]\kappa_3 - GJ(\kappa_3 - \kappa_{03})\kappa_1 + F_1 = 0, \tag{12}$$

$$GJ\left(\frac{d\kappa_3}{ds} - \frac{d\kappa_{03}}{ds}\right) - [EI_1(\kappa_1 - \kappa_{01}) + M_R]\kappa_2 + EI_2(\kappa_2 - \kappa_{02})\kappa_1 = 0. \tag{13}$$

For simplicity, the arc length s is omitted from all the variables in the governing equations and from the subsequent section unless otherwise stated.

In order to relate the local basis to the global basis and solve the equilibrium equations, a unit quaternion $\mathbf{q}(s) = [q_0(s), q_1(s), q_2(s), q_3(s)]$ with $q_0^2 + q_1^2 + q_2^2 + q_3^2 = 1$ is introduced (Healey and Mehta, 2005; Yu and Hanna, 2019), which gives

$$\begin{bmatrix} e_1 \\ e_2 \\ e_3 \end{bmatrix} = 2\begin{bmatrix} q_0^2 + q_1^2 - \frac{1}{2} & q_1q_2 + q_0q_3 & q_1q_3 - q_0q_2 \\ q_1q_2 - q_0q_3 & q_0^2 + q_2^2 - \frac{1}{2} & q_2q_3 + q_0q_1 \\ q_1q_3 + q_0q_2 & q_2q_3 - q_0q_1 & q_0^2 + q_3^2 - \frac{1}{2} \end{bmatrix}\begin{bmatrix} E_1 \\ E_2 \\ E_3 \end{bmatrix}. \tag{14}$$

Substituting e_3 from Eq. (14) into Eq. (1), the kinematic equations of the centerline expressed by the quaternion components are given by

$$\frac{dr_1}{ds} = 2(q_1q_3 + q_0q_2), \tag{15}$$

$$\frac{dr_2}{ds} = 2(q_2q_3 - q_0q_1), \tag{16}$$

$$\frac{dr_3}{ds} = 2\left(q_0^2 + q_3^2 - \frac{1}{2}\right), \tag{17}$$

where r_i ($i = 1, 2, 3$) is the component of the position vector $\mathbf{r}(s)$, and $\mathbf{r}(s) = r_1\mathbf{E}_1 + r_2\mathbf{E}_2 + r_3\mathbf{E}_3$. Taking the derivative of Eq. (14) with respect to s and then inserting it into Eq. (2), the kinematic equations describing the orientation of the cross-section can be rewritten as

$$\frac{dq_0}{ds} = \frac{1}{2}\left(-q_1\kappa_1 - q_2\kappa_2 - q_3\kappa_3\right), \tag{18}$$

$$\frac{dq_1}{ds} = \frac{1}{2}\left(q_0\kappa_1 - q_3\kappa_2 + q_2\kappa_3\right), \tag{19}$$

$$\frac{dq_2}{ds} = \frac{1}{2}\left(q_3\kappa_1 + q_0\kappa_2 - q_1\kappa_3\right), \tag{20}$$

$$\frac{dq_3}{ds} = \frac{1}{2}\left(-q_2\kappa_1 + q_1\kappa_2 + q_0\kappa_3\right). \tag{21}$$

Eqs. (8)–(13) and (15)–(21) provide 13 first-order ordinary differential equations for the rod, which contain 13 unknown variables $[F_i, \kappa_i, r_i, q_0, q_i]$ ($i = 1, 2, 3$), producing a well-posed boundary value problem when equipped with appropriate boundary conditions.

For the hexagonal ring, only one quarter of the ring is needed for the analysis due to its symmetry. However, the natural curvatures of the hexagonal ring are discontinuous at the joints of the straight edge and the rounded corner, so the quarter ring is further divided into four segments (see Fig. B1), with each segment modeled as a Kirchhoff rod. Thus, we have 52 governing equations in terms of 52 variables, i.e., $[F_1^{(j)}, F_2^{(j)}, F_3^{(j)}, \kappa_1^{(j)}, \kappa_2^{(j)}, \kappa_3^{(j)}, r_1^{(j)}, r_2^{(j)}, r_3^{(j)}, q_0^{(j)}, q_1^{(j)}, q_2^{(j)}, q_3^{(j)}]$ ($j = 1, 2, 3, 4$), for the hexagonal ring. To establish a general framework, the following nondimensional quantities are introduced,

$$\bar{s}^{(j)} = \frac{s^{(j)}}{a\ell^{(j)}}, \bar{r}_i^{(j)} = \frac{r_i^{(j)}}{a}, \left(\bar{\kappa}_i^{(j)}, \bar{\kappa}_{0i}^{(j)}\right) = \left(\kappa_i^{(j)}, \kappa_{0i}^{(j)}\right)a, \bar{F}_i^{(j)} = F_i^{(j)}\frac{a^2}{GJ}, \bar{M}_R = \frac{M_R a}{GJ}, \frac{d(\bullet)}{ds^{(j)}} = \frac{d(\bullet)}{d\bar{s}^{(j)}}\frac{1}{a\ell^{(j)}}. \tag{22}$$

Here, $\ell^{(j)} = L^{(j)}/a$ is a scaling factor unifying the dimensionless arc lengths of different segments into a same range, i.e., $\bar{s}^{(j)} \in [0, 1]$, where $L^{(j)}$ is the segment length. By using Eq. (22), the dimensionless form of the governing equations for the jth segment can be obtained, which are presented in Appendix B. In the present theoretical modeling, we consider three different loading methods to fold the hexagonal ring, which are twisting load, bending load, and point load. The boundary conditions for the hexagonal ring under these different loading methods are provided in Appendix B. For each case, 52 boundary conditions are given, which equals the number of the governing equations and unknown variables, leading to a well-posed boundary value problem. To solve it, Continuation Core and Toolboxes (COCO) (Dankowicz and Schilder, 2011, 2013), a numerical continuation package operated in MATLAB, is adopted. In the numerical solution procedure, the twisting angle Φ, the bending angle Θ, and the displacement δ are respectively chosen as the continuation parameters for the three loading methods considered. Note that we use Poisson's ratio $\nu = 0.3$, and geometric parameters of the fabricated ring with $h/t = 4$, $r/a = 0.05$ and $r/t = 10$ for all theoretical and FEA studies in this work.

2.4. Effect of residual strain

In this subsection, we use the theoretical model combined with FEA simulations and experiments to study the effect of residual strain on the snap-folding behavior of the modified hexagonal ring under twisting or bending loads. For each loading method, four different residual strains are considered ($\varepsilon_0 = 0$, 0.0026, 0.0052, and 0.0069), and the corresponding natural states of the connected rings and their disconnected counterparts are depicted in Fig. 5(a). We first study the snap-folding behavior of the modified hexagonal ring subjected to a pair of twisting moments at corners (see Fig. 5(b)). By using the rod model and FEA, we obtain the normalized moment-twisting angle curves of the modified hexagonal ring during the folding process, as illustrated in Fig. 5(c). It is seen that the results predicted by the rod model are in excellent agreement with the FEA simulations, and both results show that the hexagonal ring without residual strain is un-foldable. However, when introducing a small residual strain (e.g., $\varepsilon_0 = 0.0026$ or 0.0052), the hexagonal ring becomes foldable via the snap-through instability. Also, we can observe that as the residual strain increases, the required moment to fold the ring reduces, and the snapping point appears at smaller twisting angles. When the residual strain reaches a critical value ($\varepsilon_0 = 0.0069$), the initial state of the ring is no longer stable, and snap-back occurs when applying external twisting moments at corners. In this case, FEA is unable to capture the complete snap-back process due to the displacement-controlled loading process.

To understand how residual strain facilitates snap-folding of the ring, we investigate the energy landscape during folding by constructing the normalized strain energy-twisting angle curves of the modified hexagonal ring with different residual strains, as shown in Fig. 5(d). The theoretical derivation of the strain energy of the modified hexagonal ring is provided in Appendix C. As can be seen, the energy curve of the un-foldable ring ($\varepsilon_0 = 0$) has only one local minimum, corresponding to the zero-energy stable state in its initial configuration. The energy curves of the two foldable rings ($\varepsilon_0 = 0.0026$ and 0.0052) both have two local minima, corresponding to their two stable states in the initial configuration and the folded configuration, respectively. For each foldable ring, the energy difference between the initial state and the maximum-energy state is denoted as the energy barrier for snap-folding. For the ring with a higher residual strain ($\varepsilon_0 = 0.0052$), it has a larger initial strain energy, and thus its energy barrier ($\Delta\bar{U}_{5.2}$) is much smaller than that of
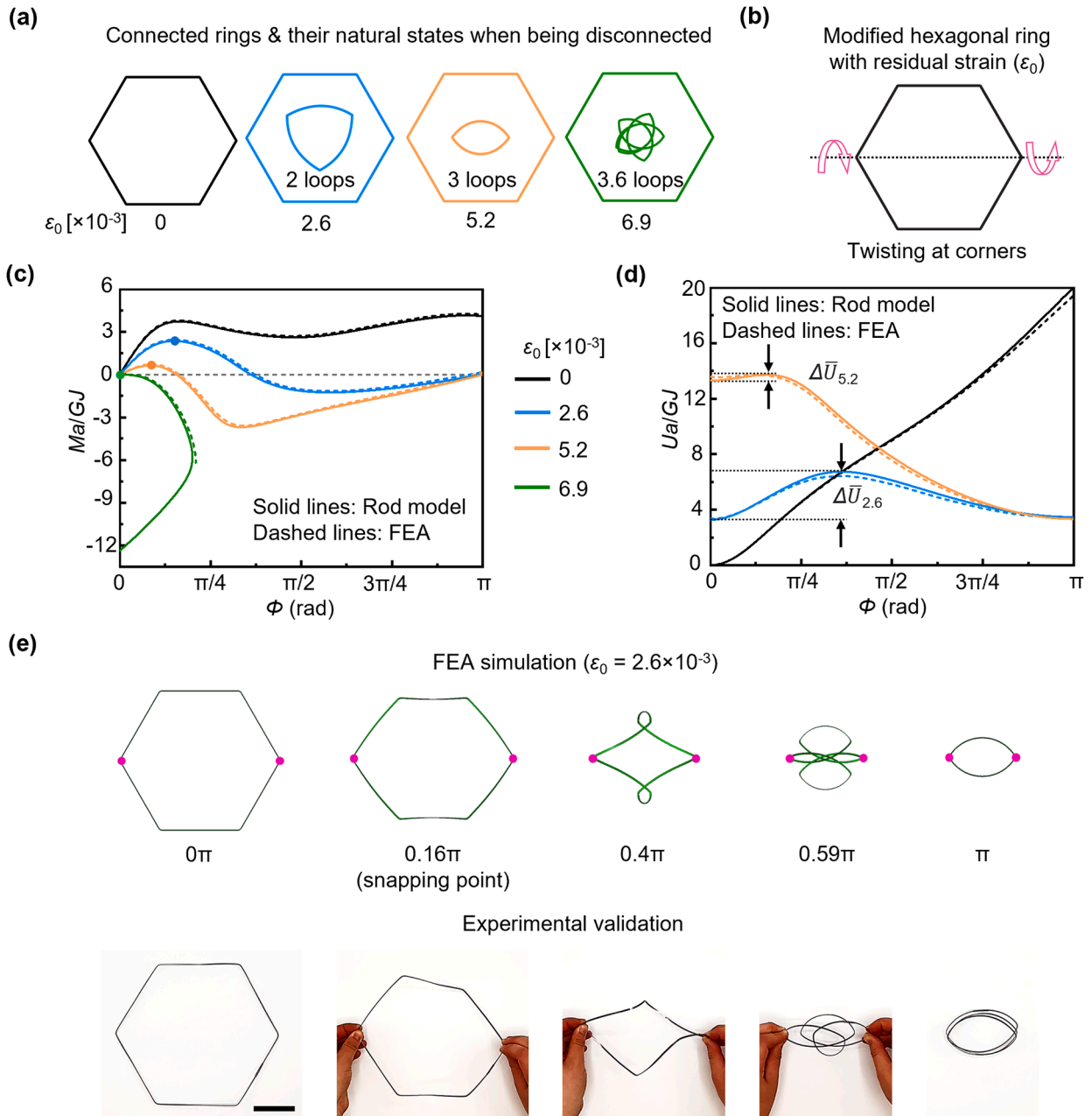
Fig. 5. Snap-folding of the modified hexagonal ring with residual strain under twisting loads at corners. (a) Geometric configurations of the connected rings with different residual strains and their natural states when being disconnected. (b) Schematic of the modified hexagonal ring under a pair of twisting moments at corners. (c) Normalized moment and (d) normalized strain energy versus twisting angle for the modified hexagonal ring with different residual strains. The dots in (c) correspond to the snapping points. (e) Folding processes of the modified hexagonal ring with residual strain ($\varepsilon_0 = 0.0026$) obtained by the FEA simulation and experiment, with the dots corresponding to the loading points. Scale bar: 50 mm.

the ring with lower residual strain ($\Delta \bar{U}_{2.6}$ with $\varepsilon_0 = 0.0026$), indicating that the ring with larger residual strain requires less energy input from the external load to overcome the energy barrier and achieve the snap-folding. In other words, the residual strain can significantly decrease the energy barrier to fold the hexagonal ring. Fig. 5(e) compares the folding processes of the modified hexagonal ring with residual strain $\varepsilon_0 = 0.0026$ obtained by the FEA simulation and the experiment. The results show good agreement by demonstrating the modified hexagonal ring folding into a peach core-shaped structure after undergoing a series of intermediate configurations.

We next study the snap-folding behavior of the modified hexagonal ring with residual strain under a pair of twisting moments at the middle of the edges (see Fig. 6(a)). The same residual strains as above are studied here. Fig. 6(b) illustrates the normalized moment-

twisting angle curve of the modified hexagonal ring predicted by the rod model and FEA. Again, our theoretical results agree with the FEA simulations very well. Moreover, it can be observed that the hexagonal ring without residual strain is foldable in this case, which means that snap-folding of the hexagonal ring is easier to achieve by twisting at edges than at corners. Similar to the previous example, the required moment to snap-fold the ring reduces with the increasing residual strain. The same critical value of the residual strain (ε_0 = 0.0069) is observed for the initial state of the modified hexagonal ring to be unstable. The normalized strain energy-twisting angle curves of the modified hexagonal ring with various residual strains are plotted in Fig. 6(c). It is shown in all the three cases that the energy curves have two energy minima, which correspond to the initial stable state and the folded stable state, respectively. Meanwhile, the residual strain largely decreases the energy barrier ($\Delta \bar{U}_{2.6}$ and $\Delta \bar{U}_{5.2}$) of the modified hexagonal ring, making it easier to fold. Fig. 6(d) presents the folding process of the modified hexagonal ring with residual strain ε_0 = 0.0026 under a pair of twisting moments at the middle of the edges. It is seen that the FEA simulation nicely predicts the folding process of the ring in the experiment.

Additionally, results for the snap-folding of the modified hexagonal ring with different residual strains under a pair of bending moments at corners or at edges are presented in Fig. D1 in Appendix D. Similar conclusions can be drawn from the bending cases. As a conclusion, introducing residual strain is demonstrated to fold the ring effectively and easily, as it decreases the energy barrier and thus reduces the required moment to trigger snap-folding, while bringing the onset of snapping to an earlier stage.

3. Modified hexagonal ring with pre-twisted edges

Creating pre-twisted edges has been found to have a considerable influence on the instabilities of rod-like or ring-like structures (Goriely, 2006; Neukirch et al., 2002). In this section, we will investigate how pre-twisted edges change the snap-folding of the hexagonal ring, and conduct FEA simulations and theoretical modeling to quantitatively study the effects of pre-twisted edges as well as its coupling with residual strain on the snap-folding of the modified hexagonal ring.

3.1. Finite element simulations

In the current work, the pre-twisted edges of the modified hexagonal ring are created by applying a pair of torques to each straight edge of a regular hexagonal ring. As shown in Fig. 7(a), the red and blue dots are the applied torque locations, which are at the two ends of the straight edges. The torques are along the longitudinal direction of each straight edge. Following the right-hand rule, the positive torque direction is defined as the direction of the torsion axis perpendicular to and outward from the ring's cross-section, as shown in Fig. 7(b). To simulate the snap-folding behavior of the modified hexagonal ring with pre-twisted edges (Fig. 7(c)), we first prescribe a pair of pre-twisted angles (γ) at the two ends of each straight edge (Fig. 7(b)) and obtain its deformed configuration. Then, the deformed configuration is exported without stress to serve as the initial geometry of the modified hexagonal ring. Finally, the folding of the modified hexagonal ring is simulated by applying twisting or bending loads.

3.2. Theoretical modeling

In the theoretical modeling, the Kirchhoff rod model derived in Section 2 still applies, while the initial bending curvatures and twisting curvatures which define the initial configuration of the hexagonal ring need to be modified to precisely describe the geometric modification of the ring. To achieve this, we first find the analytical description of the bending curvatures and the twisting curvature of the modified hexagonal ring with pre-twisted edges. For the straight edges, the pre-twisted angle linearly varies along the longitudinal direction when subjected to a constant torque at the two ends. At the rounded corners, it is difficult to give an accurate analytical description for the twisting angle variation along the arc length. However, since the size of the rounded corner is much smaller than that of the straight edge, the variation of the pre-twisted angle at the rounded corner has little effect on the snap-folding behavior of the modified hexagonal ring. For convenience, we assume that the pre-twisted angle also linearly changes along the arc length at the rounded corners. In this way, when the bending or twisting loads are applied at corners of the modified hexagonal ring (see Fig. B1(a)), variation of the pre-twisted angle in the *j*th (*j* = 1, 2, 3, 4) segment can be written as

$$\varphi^{(j)} = \begin{cases} -\dfrac{2\gamma}{c}s^{(1)}, s^{(1)} \in \left[0, \dfrac{c}{2}\right] \\[2mm] \dfrac{6\gamma}{\pi r}s^{(2)} - \gamma, s^{(2)} \in \left[0, \dfrac{\pi r}{3}\right] \\[2mm] -\dfrac{2\gamma}{c}s^{(3)} + \gamma, s^{(3)} \in [0, c] \\[2mm] \dfrac{6\gamma}{\pi r}s^{(4)} - \gamma, s^{(4)} \in \left[0, \dfrac{\pi r}{6}\right] \end{cases} \tag{23}$$

Here, γ is the pre-twisted angle which is applied at the two ends of the straight edge, c is the length of the straight edge, and $c = a - 2r/\sqrt{3}$. When the bending or twisting loads are applied at edges of the modified hexagonal ring (see Fig. B1(b)), variations of the pre-twisted angle in different segments can be obtained in a similar way. With the analytical description of the pre-twisted angle, the initial bending curvatures and twisting curvature of the modified hexagonal ring at each segment can be calculated as follows:
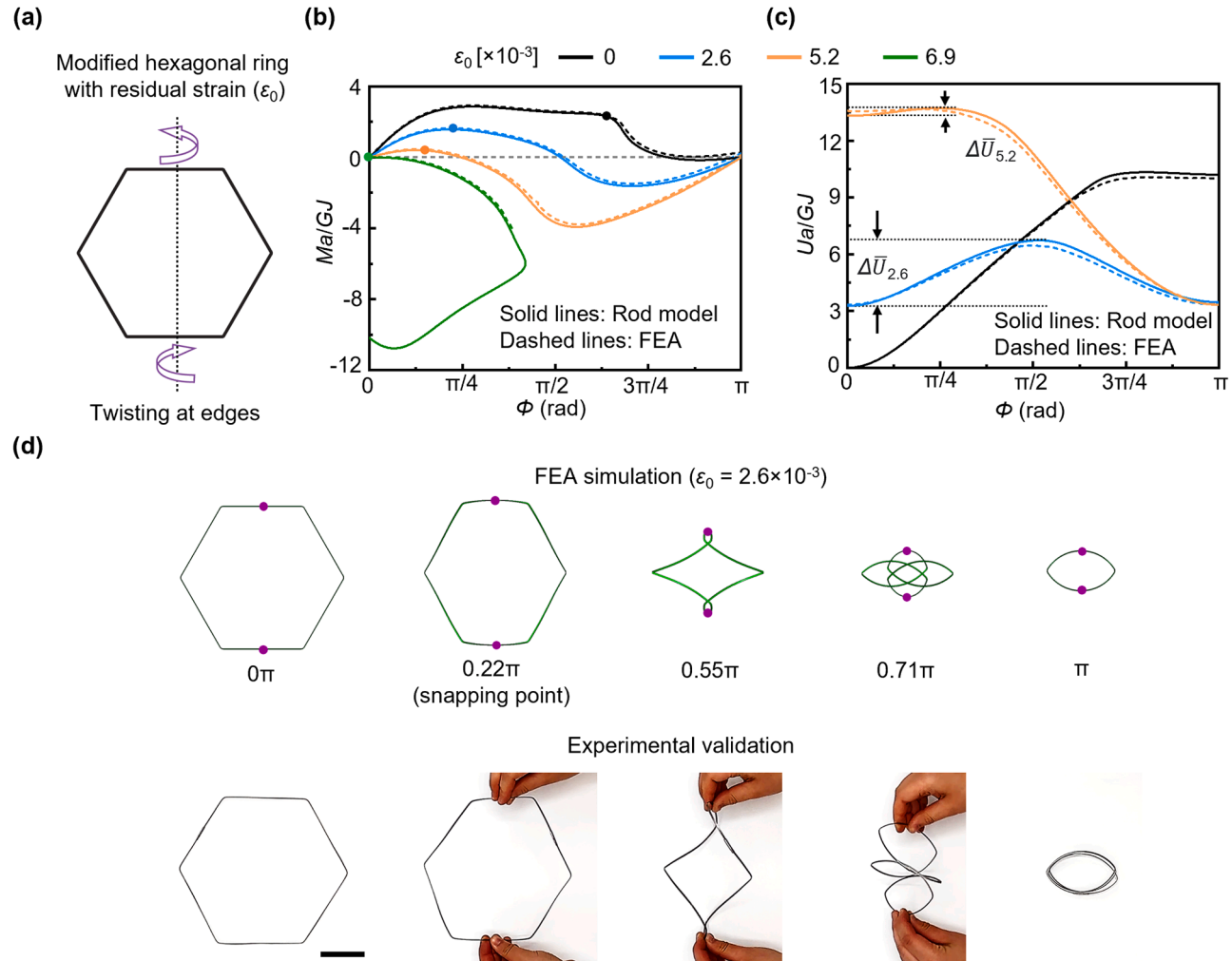
Fig. 6. Snap-folding of the modified hexagonal ring with residual strain under twisting loads at edges. (a) Schematic of the modified hexagonal ring under a pair of twisting moments at edges. (b) Normalized moment and (c) normalized strain energy versus twisting angle for the modified hexagonal ring with different residual strains. The dots in (b) correspond to the snapping points. (d) Folding processes of the modified hexagonal ring with residual strain ($\varepsilon_0 = 0.0026$) obtained by the FEA simulation and the experiment, with the dots corresponding to the loading points. Scale bar: 50 mm.
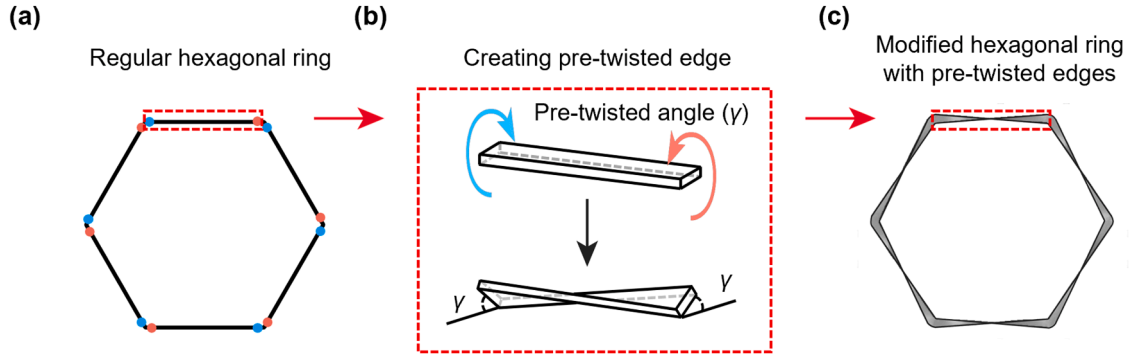
Fig. 7. FEA simulations and theoretical modeling of the modified hexagonal ring with pre-twisted edges. (a) Regular hexagonal ring with two ends of each edge highlighted by the blue and red dots. (b) A pair of torques is applied to the two ends of each straight edge to plastically pre-twist the edge. The positive torque directions are illustrated by the arrows. (c) Schematic of the modified hexagonal ring with pre-twisted edges.

$$\left(\kappa_{01}^{(j)}, \kappa_{02}^{(j)}, \kappa_{03}^{(j)}\right) = \left(\kappa^{(j)}\cos\varphi^{(j)}, -\kappa^{(j)}\sin\varphi^{(j)}, \tau^{(j)} + \frac{d\varphi^{(j)}}{ds^{(j)}}\right), \tag{24}$$

in which $\kappa^{(j)}$ and $\tau^{(j)}$ are the Frenet curvature and torsion (Moulton et al., 2013) of the regular hexagonal ring. Particularly, for straight edges, we have $\kappa^{(j)} = 0$ and $\tau^{(j)} = 0$, which means the pre-twist in the longitudinal direction does not affect the bending curvature in the other two directions, while at rounded corners, we have $\kappa^{(j)} = 1/r$ and $\tau^{(j)} = 0$, which indicates the pre-twist has influence on the other two curvatures. With the initial curvature information, the Kirchhoff rod model is then ready to provide the fundamental insight into the snap-folding behavior of the modified hexagonal ring with pre-twisted edges under different loading methods. It should be mentioned that when using the bending method to fold the modified hexagonal ring with pre-twisted edges, one quarter of the ring is no longer sufficient for the analysis, as the ring is geometrically antisymmetric while the external load is symmetric about the bending axis. Theoretical framework of the bending cases can be obtained using the rod model by considering a whole hexagonal ring being divided into 14 segments (4 segments for the edges or corners where the bending loads are applied, and 10 segments for the remaining unloaded edges and corners).

3.3. Effect of pre-twisted edges

In the following, we use the theoretical model and FEA to investigate the effect of pre-twisted edges on the snap-folding behavior of the modified hexagonal ring under twisting loads. Following the right-hand rule, we define the twisting direction with its axis pointing inward to the center of the ring as "negative twisting", as shown in Figs. 8(a) and 9(a), and pointing outwards as "positive twisting", as shown in Figs. 8(b) and 9(b). Moreover, to avoid confusion, we define the twisting angle and the pre-twisted angle as follows: the twisting angle corresponds to the angle change at the loading points when the twisting loads are applied, while the pre-twisted angle denotes the longitudinal twist at the two ends of straight edges (geometric modification) of the ring in its initial state.

The modified hexagonal ring with pre-twisted edges subjected to a pair of negative twisting moments at corners (see Fig. 8(a)) is first studied by the theoretical model and FEA simulations. Fig. 8(c) shows the normalized moment-twisting angle curves of the modified hexagonal ring with different pre-twisted angles of the edges ($\gamma = 0°$, 15°, 30°, and 45°), and the corresponding folding processes are shown in Fig. D2 in Appendix D. One can find that the un-foldable regular ring ($\gamma = 0°$) under twisting loads at corners becomes foldable when inducing pre-twisted edges by a small angle (e.g., $\gamma = 15°$), indicating that pre-twisted edges facilitate the folding of the modified hexagonal ring. However, as the pre-twisted angle increases, the snapping point tends to appearlater, while the required twisting moments to snap-fold the ring remain the same. The normalized strain energy-twisting angle curves are shown in Fig. 8(d). It is seen that the strain energy of the un-foldable regular ring monotonically increases with the twisting angle. On the other hand, for the modified hexagonal rings with pre-twisted edges, their energy curves first increase and then reach their plateaus when snap-folding takes place. In particular, when the pre-twisted angle γ equals 15°, the energy curve has two energy minima, corresponding to the two stable states at the initial and folded configurations. However, as the pre-twisted angle increases (e.g., $\gamma = 30°$ or 45°), the ring is still foldable, but it is no longer stable at the folded state. This suggests that inducing only a slight pre-twist to the edges helps with snap-folding of the ring, while a larger pre-twist can affect the stability of the folded ring. We further examine the folding behavior of the modified hexagonal ring with pre-twisted edges under a pair of positive twisting moments at corners (see Fig. 8(b)), and show the normalized moment and strain energy versus the twisting angle curves for different pre-twisted angles in Fig. 8(e) and (f), respectively. In this case, the initially un-foldable hexagonal ring is still un-foldable after introducing the pre-twisted edges (see Fig. D3 in Appendix D for the deformation configurations of the folding processes). However, lower moment and strain energy are observed for the modified hexagonal ring with larger pre-twisted angles of the edges.

Next, snap-folding behavior of the modified hexagonal ring with pre-twisted edges under a pair of twisting moments at edges is studied in Fig. 9. We consider the same twisting directions, i.e., negative twisting (Fig. 9(a)) and positive twisting (Fig. 9(b)). The normalized moment-twisting angle curves for different pre-twisted angles in these two cases are given in Fig. 9(c) and Fig. 9(e), and the
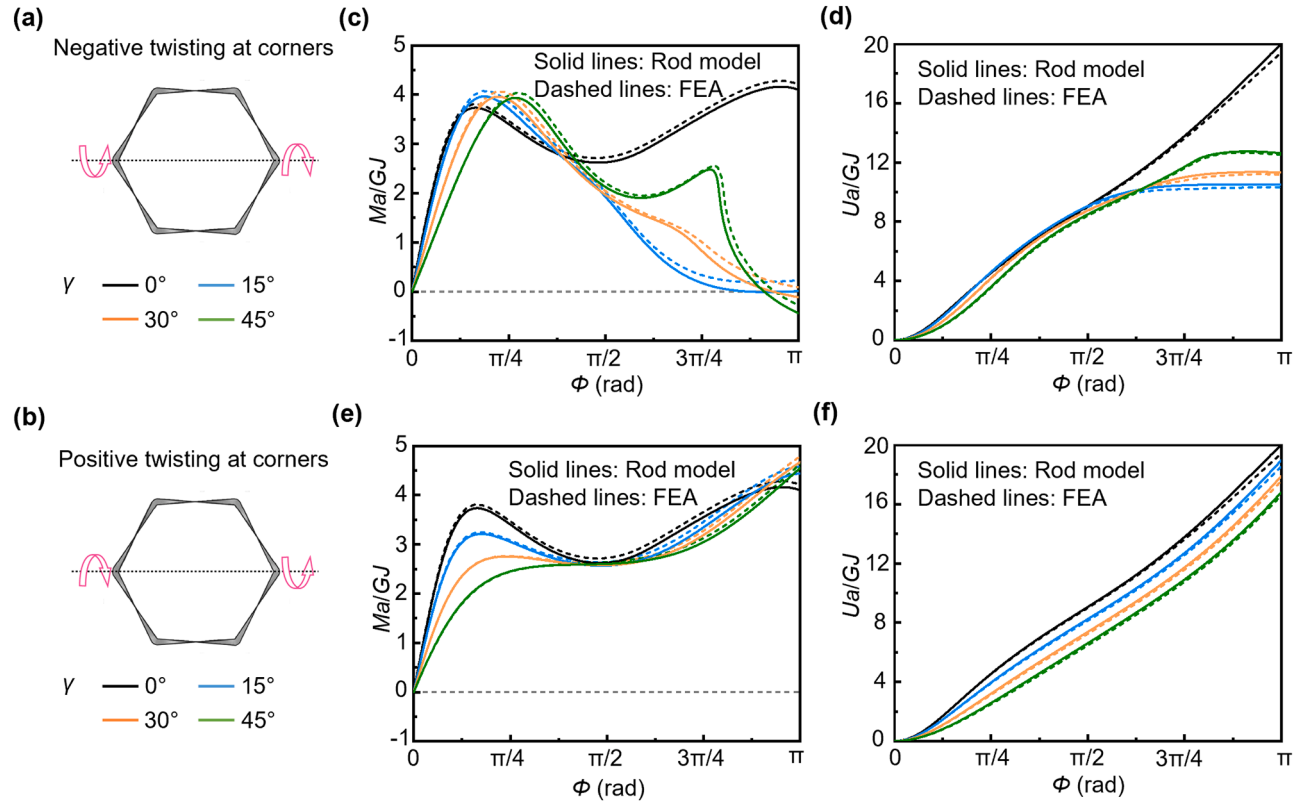
Fig. 8. Snap-folding of the modified hexagonal ring with pre-twisted edges under a pair of twisting moments at corners. (a,b) Schematics of the modified hexagonal ring under negative (a) and positive (b) twisting loads at corners. (c,e) Normalized moment versus twisting angle for the modified hexagonal ring with different pre-twisted angles under nega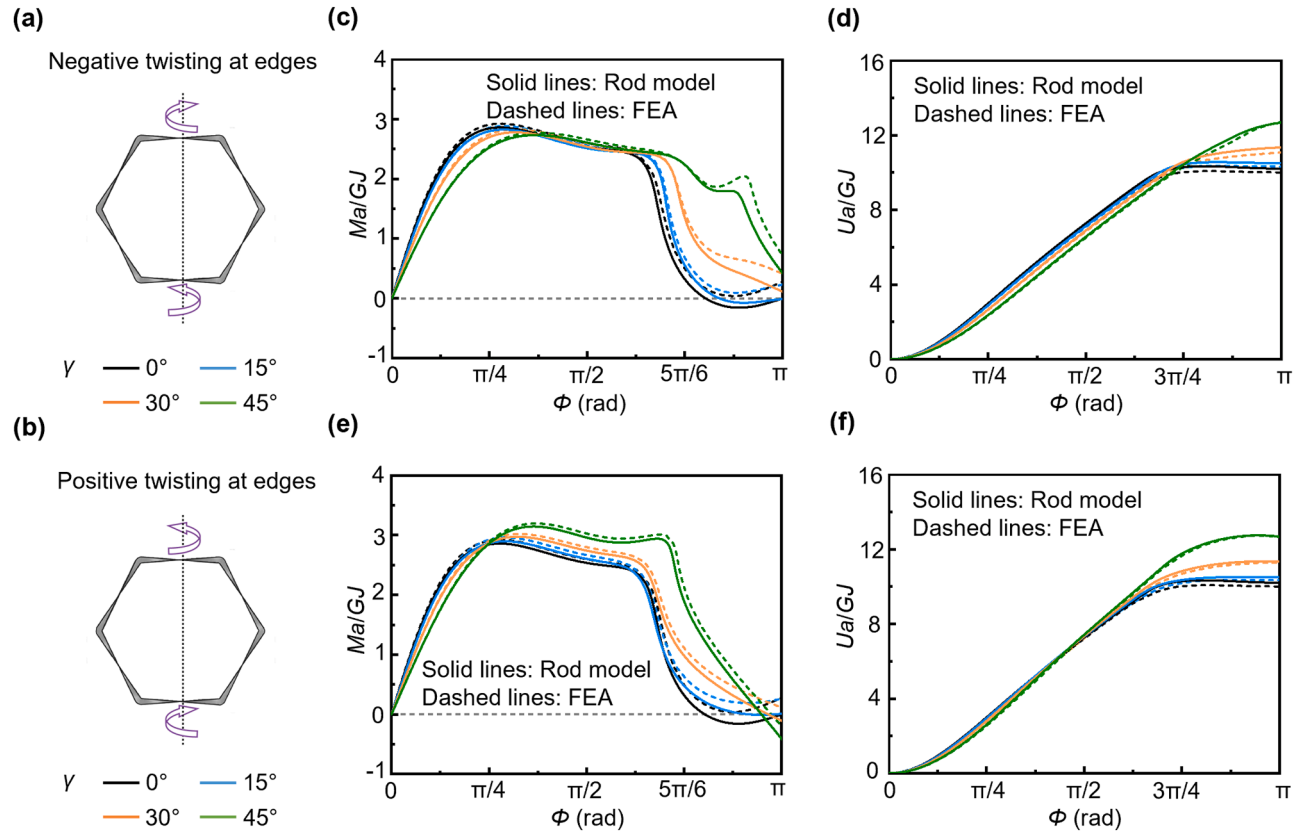tive (c) and positive (e) twisting loads at corners. (d,f) Normalized strain energy versus twisting angle for the modified hexagonal ring with different pre-twisted angles under negative (d) and positive (f) twisting loads at corners.

Fig. 9. Snap-folding of the modified hexagonal ring with pre-twisted edges under a pair of twisting moments at edges. (a,b) Schematics of the modified hexagonal ring under negative (a) and positive (b) twisting loads at edges. (c,e) Normalized moment versus twisting angle for the modified hexagonal ring with different pre-twisted angles under negative (c) and positive (e) twisting loads at edges. (d,f) Normalized strain energy versus twisting angle for the modified hexagonal ring with different pre-twisted angles under negative (d) and positive (f) twisting loads at edges.

corresponding deformation configurations during folding processes are provided in Figs. D4 and D5. It is seen that when the twisting loads are applied at edges, the hexagonal ring is always foldable, regardless of the twisting direction and the magnitude of the pre-twisted angle. Moreover, increasing the pre-twisted angle slightly delays the snapping point. The normalized strain energy-twisting angle curves for the modified hexagonal ring under negative and positive twisting loads are presented in Fig. 9(d) and Fig. 9(f), respectively. From the energy landscape, we can see that both the regular ring ($\gamma = 0°$) and the modified ring with pre-twisted angle $\gamma = 15°$ have stable folded states due to their local energy minimum at the folded configuration. For large pre-twisted angle $\gamma = 30°$ or $45°$, the folded configuration of the ring is no longer stable. FEA results for snap-folding of the modified hexagonal ring with pre-twisted edges under a pair of bending moments are provided in Fig. D6 in Appendix D. In this case, the bending direction has no influence on the folding behavior of the modified hexagonal ring. It is shown that the modified rings with different pre-twisted angles of the edges are all foldable when bending loads are applied at either corners or edges, but the snapping points slightly delay and the required moments to fold slightly increase with the increasing pre-twisted angles.

3.4. Effect of coupled residual strain and pre-twisted edges

So far, we have shown that, when the hexagonal ring is subjected to a pair of twisting or bending moments, introducing residual strain and pre-twisted edges can both facilitate folding. However, the ability of modified rings to enable folding under easier loading methods is not yet exploited. In this subsection, we will demonstrate that, by introducing the residual strain and pre-twisted edges simultaneously, the snap-folding of the hexagonal ring can be achieved either by no external mechanical loads or by just applying a point load.

Without any external load, we first show the snap-folding behavior of the modified hexagonal ring with pre-twisted edges under increasing residual strain. In this case, the pre-twisted angle is prescribed (i.e., $\gamma = 15°$, $30°$, $45°$), while the residual strain continuously increases from 0 by increasing the corresponding thermal strain in FEA simulations. Fig. 10(a) shows the normalized strain energy versus the residual strain for rings with different pre-twisted angles of the edges predicted by FEA simulations. As expected, the strain energy first increases with the increasing residual strain. When the residual strain reaches a critical value, the strain energy drops suddenly, which corresponds to the snap-folding behavior. The geometric configurations of the modified hexagonal ring during snapping are shown in Fig. 10(b). Points A, C, and E correspond to the incipient states of snapping, and points B, D, and F correspond to the folded states at the local energy minima. For the three pre-twisted angles considered, the deformation configurations of the rings during snap-folding are similar to one another. It is shown that the rings barely deform before the snapping point, but rapidly collapse to the peach core shape at the snapping point. To better illustrate this, a complete folding process corresponding to $\gamma = 15°$ is provided in Movie 4 in Supplementary Materials. This result demonstrates that a modified hexagonal ring with pre-twisted edges can snap-fold just from a gradual increase in the residual strain without the need for external twisting or bending moments. The increasing of residual strain can potentially be experimentally achieved by manufacturing rings with active materials such as thermally responsive materials that provide strain upon temperature change (Bae et al., 2014; Peng et al., 2022; Roach et al., 2022; Sun et al., 2022b; Ze et al., 2020). Furthermore, we can find from Fig. 10(a) that the modified ring with larger pre-twisted angles requires a smaller critical residual strain to trigger the snap-folding, as large pre-twisted angles are more easily able to induce out-of-plane deformation.

In applications of ring origami-based large-scale functional structures, it is usually desirable to fold the whole structure in a simple manner. Compared to folding by twisting or bending loads which requires two loading points, much simpler loads such as a point load is preferred. Here, we study how residual strain and pre-twisted edges of the modified hexagonal ring enable snap-folding under a simple point load. As shown in Fig. 11(a), a point load is applied to the corner of a modified hexagonal ring. The residual strain in the ring is set as $\varepsilon_0 = 0.0039$, which corresponds to the 2.5-loop natural state when being disconnected. The pre-twisted angles of the edges are varied from $0°$ to $45°$. Fig. 11(b) shows the normalized force-displacement curves of the modified hexagonal ring under a point load with different pre-twisted angles of the edges predicted by the rod model and FEA. The force P is normalized by the edge length a and
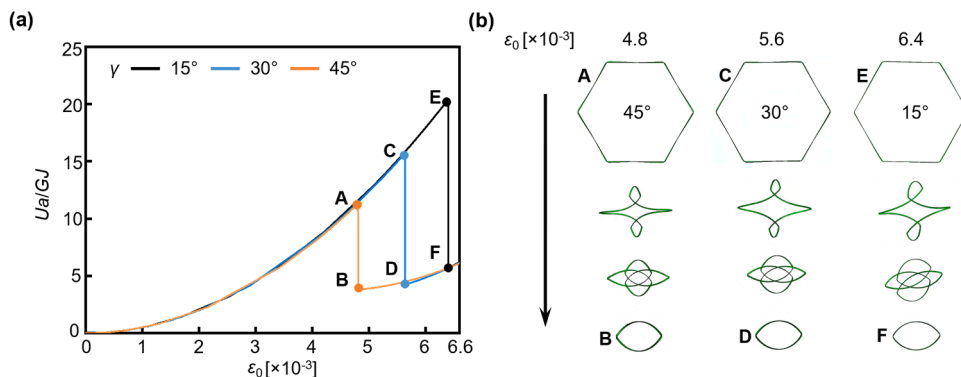

Fig. 10. Snap-folding of the modified hexagonal ring with pre-twisted edges driven by an increasing residual strain predicted by FEA simulations. (a) Normalized strain energy versus residual strain for rings with different pre-twisted angles. (b) Snap-folding processes of the modified hexagonal ring with different pre-twisted angles of the edges triggered by increasing residual strain.
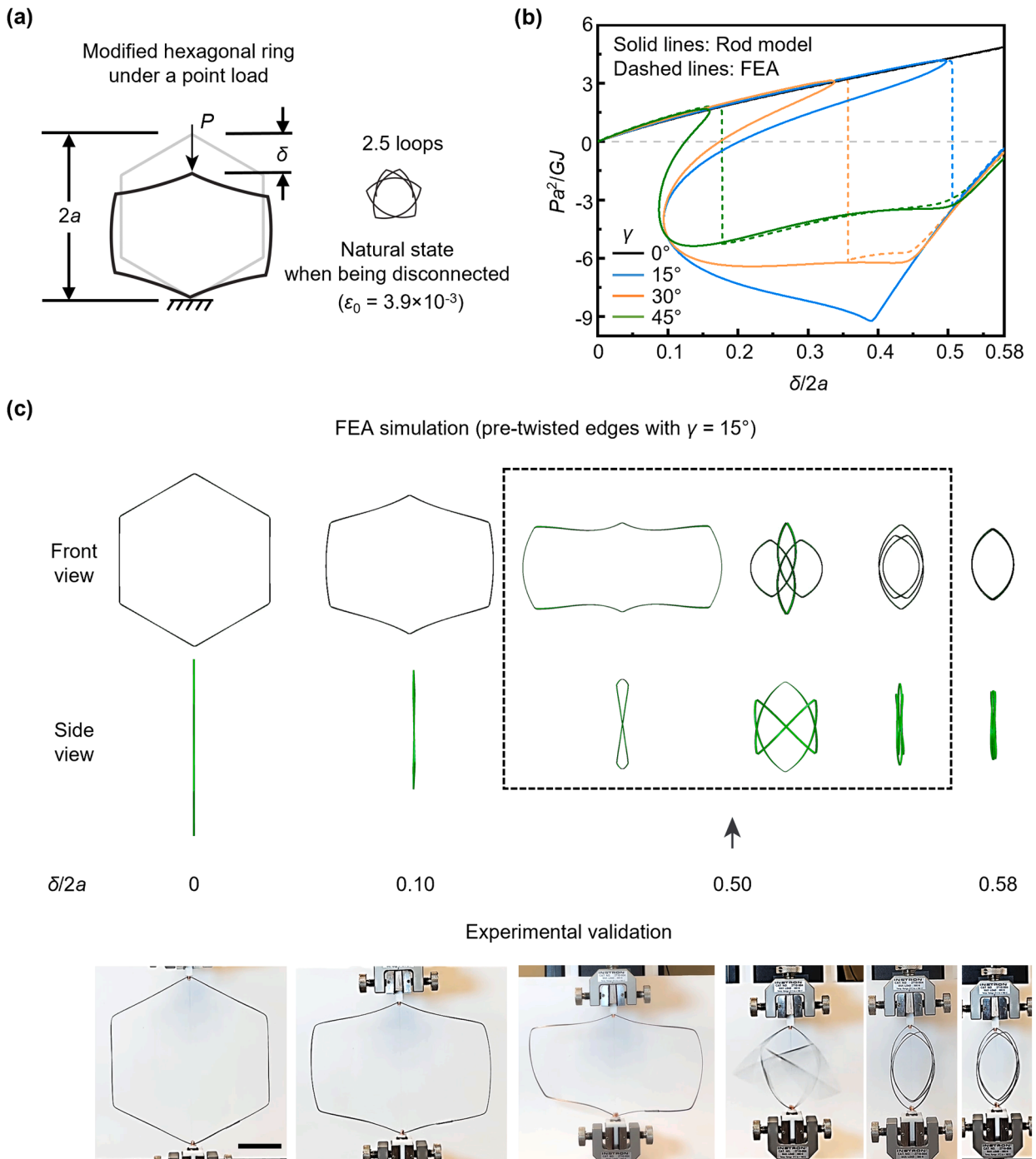
Fig. 11. Snap-folding of the modified hexagonal ring with pre-twisted edges and residual strain under a point load. (a) Schematic of the modified hexagonal ring under a point load. (b) Normalized point force versus the displacement for the modified hexagonal ring with residual strain and different pre-twisted angles. (c) Folding processes of the modified hexagonal ring with residual strain ($\varepsilon_0 = 0.0039$) and pre-twisted edges ($\gamma = 15°$) under a point load obtained by the FEA simulation and experiment. Scale bar: 50 mm.

the torsional rigidity GJ, and the displacement δ is normalized by $2a$. It is seen that the modified hexagonal ring with only residual strain but no pre-twisted edges (i.e., $\gamma = 0°$) is un-foldable, as a point load cannot trigger out-of-plane deformation for a ring without pre-twist. However, when introducing pre-twisted edges (i.e., $\gamma = 15°$, $30°$, and $45°$), the modified hexagonal ring with residual strain becomes foldable, and snap-folding occurs when the external force reaches a critical value. Note that the rod model captures the snap-back behavior of the ring during folding, which cannot be obtained by FEA simulations or experiment due to the displacement-controlled loading process. Fig. 11(c) shows the FEA and experimental folding processes of the modified hexagonal ring with both residual strain ($\varepsilon_0=0.0039$) and pre-twisted edges ($\gamma = 15°$) under a point load. As can be seen, both results show the same snap-folding process of the modified hexagonal ring. Particularly, it can be seen from the side view of the folding process in the FEA simulation that the modified ring initially only exhibits in-plane contraction, like that of the regular ring. However, with an increasing force, the pre-twisted edges facilitate the generation of out-of-plane twisting, causing the ring to snap to the peach core shape. The folding process of the modified hexagonal ring predicted by the rod model is provided in Fig. D7 in Appendix D. We can find that the deformed configurations of the modified ring before (configurations ①, ② and ③) and after (configurations ⑨ and ⑩) snapping obtained by the rod model are in excellent agreement with those of FEA simulation and experiment. Additionally, results shown in Fig. 11(b) indicate that increasing the pre-twisted angle of the edges decreases the required force to trigger snap-folding, making the snapping point appear earlier. It should be noted that the modified hexagonal ring with only pre-twisted edges but no residual strain, or a relatively small residual strain is un-foldable under a point load (see Fig. D8(a) in Appendix D for the case with pre-twisted edges only and Fig. D8(b) for the case with $\varepsilon_0=0.0026$, $\gamma = 15°$). Therefore, a sufficiently large residual strain is necessary to be coupled with the pre-twisted edges to decrease the energy barrier for snap-folding of the ring under a point load.

The previous studies in this section focus on the folding of modified hexagonal rings with pre-twisted edges when the rings are under increasing residual strain and point load. It is also interesting to explore the snap-folding under twisting or bending loads for modified rings with coupled residual strain and pre-twisted edges. In Fig. 12, the normalized moment-twisting angle curves of the modified hexagonal rings under negative twisting at corners (Fig. 12(a)), negative twisting at edges (Fig. 12(b)), positive twisting at corners (Fig. 12(c)), and positive twisting loads at edges (Fig. 12(d)) are illustrated for various pre-twisted angles ($\gamma = 0°$, $15°$, $30°$, and $45°$). Residual strain is prescribed as $\varepsilon_0 = 0.0026$, which corresponds to a 2-loop natural state when being disconnected. It is seen for all cases that the required moment to trigger the snap-folding reduces with the increase of the pre-twisted angle of the edges when residual
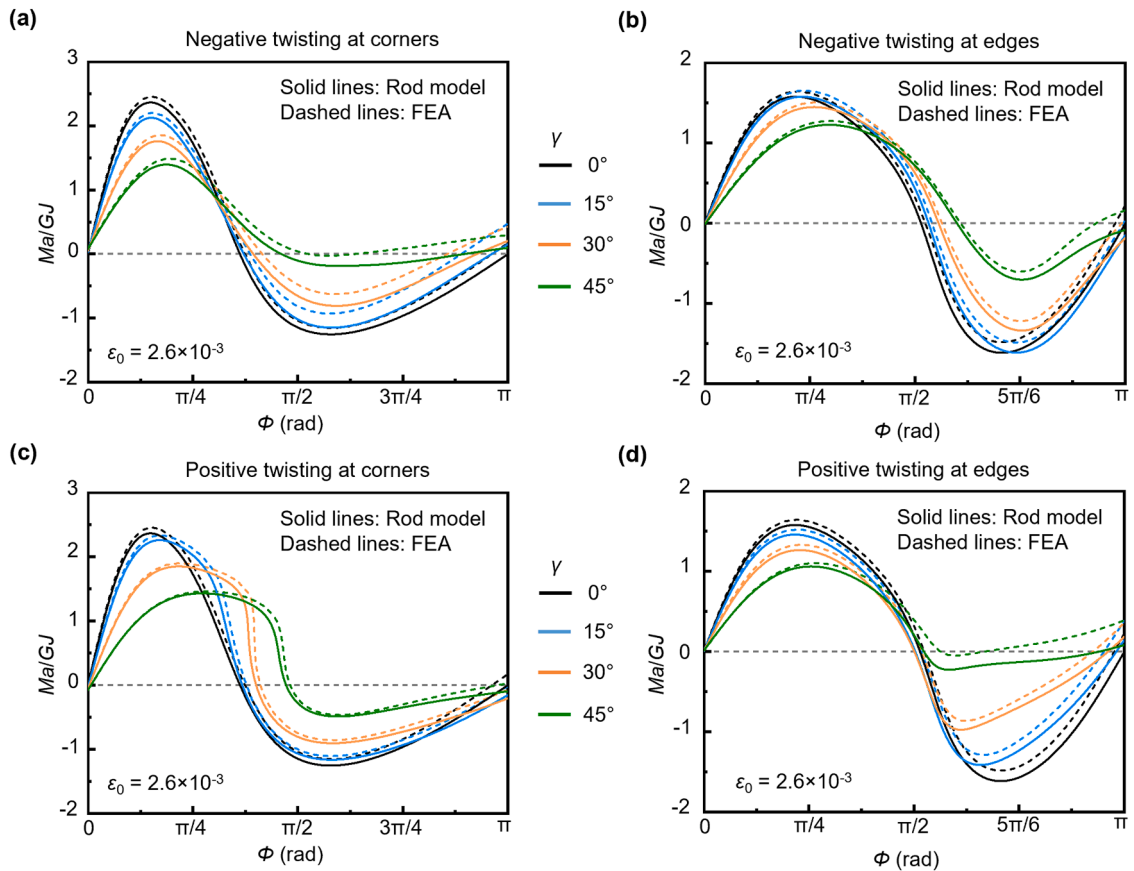

Fig. 12. Normalized moment versus twisting angle for the modified hexagonal ring with residual strain ($\varepsilon_0 = 0.0026$) and different pre-twisted angles under (a) negative twisting loads at corners, (b) negative twisting loads at edges, (c) positive twisting loads at corners, and (d) positive twisting loads at edges.
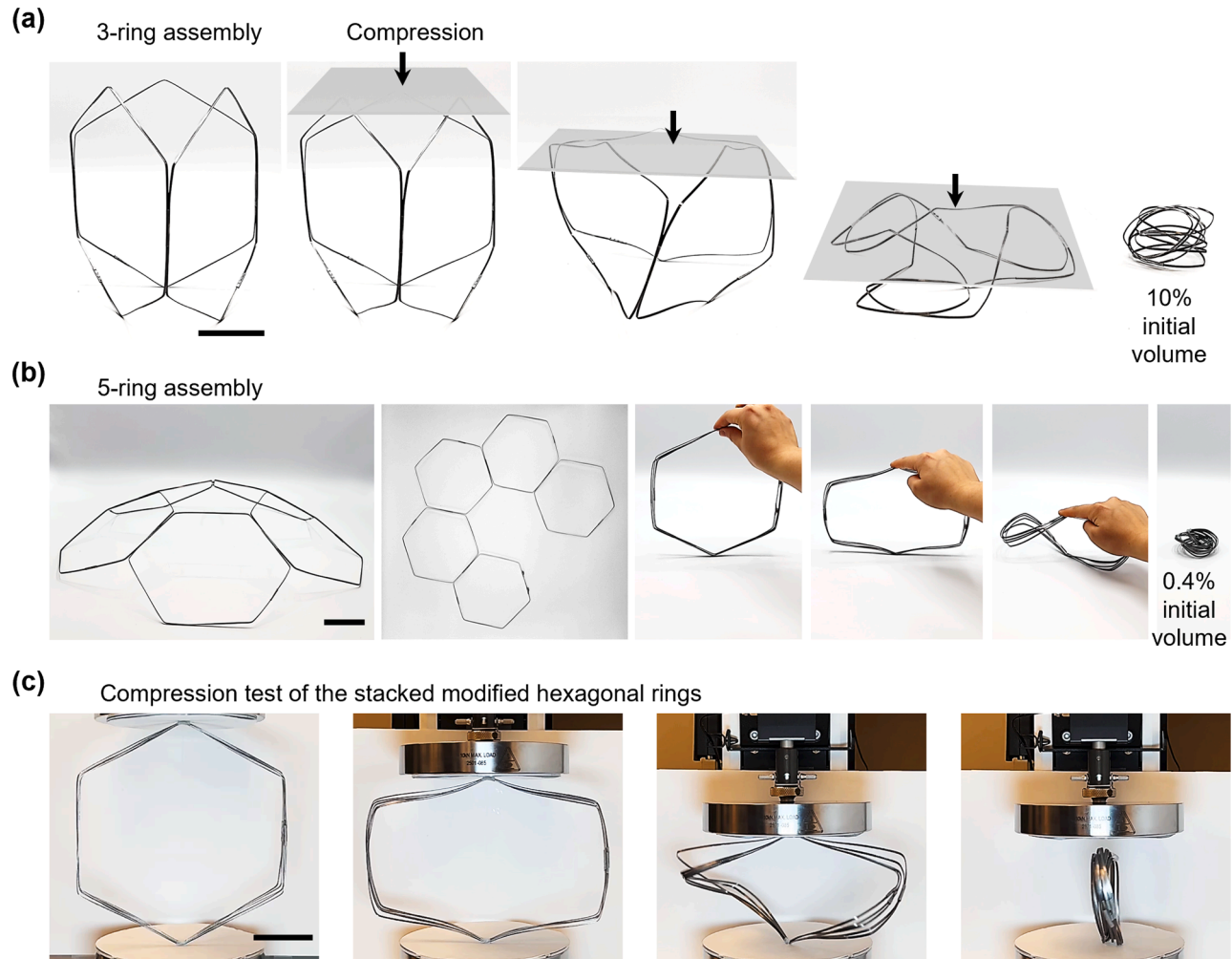
Fig. 13. Snap-folding of assemblies of modified hexagonal rings under point loads. (a) Folding process of a 3-ring assembly under point loads. A glass plate is placed on the top of the 3-ring assembly to apply point loads to the three corners simultaneously. (b) Folding process of a 5-ring assembly under a point load. The 5-ring assembly is first detached to the flat state, and then stacked to apply a point load. (c) Compression test of the stacked modified hexagonal rings on an Instron machine. Scale bars: 50 mm.

strain is added to the ring, indicating that coupled residual strain and pre-twisted edges can facilitate the snap-folding of the modified hexagonal ring under twisting loads regardless of the loading direction and loading position. Snap-folding of the modified hexagonal ring with residual strain and pre-twisted edges under bending loads at different positions is examined using FEA simulations in Fig. D9 in Appendix D. In the case of bending, we also find that increasing the pre-twisted angle tends to decrease the required moment to fold the modified hexagonal ring with residual strain.

4. Assemblies of modified hexagonal rings

Finally, we present two assemblies of the modified hexagonal ring (with both residual strain and pre-twisted edges) to demonstrate its advantages in the application of 3D foldable structures. The first one is a 3-ring assembly, which is made from three modified hexagonal rings by connecting their edges through tape hinges. In Fig. 13(a), we show the folding process of the 3-ring assembly under point loads (see Movie 5 in Supplementary Materials for details). To apply the same point load at the three top corners simultaneously, we place a glass plate on the top of the 3-ring assembly and slowly lower the glass plate. It is observed that the rings first experience an overall twisting, and then snap-fold to a 3D state with only 10% (Leanza et al., 2022) of its initial volume, which demonstrates that pre-twisted edges indeed facilitate out-of-plane deformation to trigger the snap-folding of the ring by a point load. Fig. 13(b) shows a dome-like assembly composed of five modified hexagonal rings. To fold the dome, we first flatten the 3D dome by detaching one of the hinges, and stack the rings into five overlapping rings. Then, we apply a point load to the corner of the stacked modified hexagonal rings, after which they collapse into a fully folded peach core-shaped state that is only 0.4% (Leanza et al., 2022) of the initial volume of the dome (see Movie 5 in Supplementary Materials). The compression test of the stacked rings using an Instron machine is also presented in Fig. 13(c) and Movie 6 in Supplementary Materials. We can see that when applying uniaxial compression to one corner of the stacked rings, the rings first undergo in-plane contraction. Once the load reaches a critical value, an obvious twisting of the rings is observed, which is enabled by the pre-twisted edges. The twisting is immediately followed by the snapping of the rings to reach the close-packed folded peach core configuration. It should be stated that the modified hexagonal ring assemblies not only can be folded into a small volume state, but also can be re-deployed to their initial configuration with the help of bending or twisting loads. The success of folding the two ring assemblies under point loads demonstrates that combined residual strain and pre-twisted edges are effective strategies to design ring origami-based functional structures with impressive packing abilities and easy folding.

5. Conclusion

In this work, we studied the effects of residual strain and pre-twisted edges on the snap-folding behavior of the modified hexagonal ring by combining theoretical modeling, FEA simulations, and experiments. The residual strain comes from a bending moment applied to form the hexagonal ring, and is quantified by using the equivalent thermal strain of a bilayer disconnected hexagonal ring in FEA simulations. The pre-twisted edges are created by applying a pair of torques to the two ends of each edge, and characterized by prescribing the pre-twisted angle. The Kirchhoff rod theory is employed to model the snap-folding behavior of the modified hexagonal ring under different loading methods, and its reliability is validated by comparing with the FEA results. It is found that both the residual strain and pre-twisted edges can facilitate the folding of the hexagonal ring. Specifically, residual strain can reduce the required moment to trigger the snap-folding, while pre-twisted edges can induce out-of-plane deformation to help the ring to fold. When introducing them into the hexagonal ring simultaneously, the modified hexagonal ring can be snap-folded by simply a point load or localized twist or squeeze. To demonstrate the advantages of our design strategy, we fabricate various assemblies of the modified hexagonal rings. Compared to assemblies composed of regular hexagonal rings whose snap-folding requires twisting or bending, assemblies which utilize modified rings can be easily snap-folded to small-volume states just by compressing their corners. The proposed geometric modifications provide effective design strategies to achieve the easy folding of ring origami-based functional structures with extremely high packing ratio, which have broad applications in the fields of space structures, architecture engineering, and biomedical devices.

Declaration of Competing Interest

The authors declare that they have no known competing financial interests or personal relationships that could have appeared to influence the work reported in this paper.

Data availability

Data will be made available on request.

Supplementary materials

Supplementary material associated with this article can be found, in the online version, at doi:10.1016/j.jmps.2022.105142.

Appendix A. Quantification of the residual strain

The residual strain used in the rod model is converted from the thermal strain applied in FEA simulations. For the bilayer ring considered in FEA simulations, the thermal stresses are uniformly distributed in both layers, whose resultant force and moment can be obtained as

$$F_{\mathrm{T}} = \int_{-h/2}^{h/2} \int_{-t/2}^{0} \sigma_{\mathrm{T}} dx dz + \int_{-h/2}^{h/2} \int_{0}^{t/2} (-\sigma_{\mathrm{T}}) dx dz = 0, \tag{A.1}$$

$$M_{\mathrm{T}} = \int_{-h/2}^{h/2} \int_{-t/2}^{0} \sigma_{\mathrm{T}} x dx dz + \int_{-h/2}^{h/2} \int_{0}^{t/2} (-\sigma_{\mathrm{T}}) x dx dz = -\frac{1}{4}\sigma_{\mathrm{T}} h t^2 = -\frac{1}{4} E \varepsilon_{\mathrm{T}} h t^2, \tag{A.2}$$

in which σ_{T} represents the thermal stress induced by the thermal strain ε_{T}.

For the hexagonal ring in the experiment, the residual strain is linearly distributed along the thickness, as shown in Fig. 4(b), with ε_0 being the maximum residual strain, which is on the surface of the ring. Therefore, the corresponding residual stress is also linearly distributed in the thickness, and it equals zero along the neutral axis, which is the centerline of the rectangular cross-section. Then, the distribution of the residual stress along the thickness can be described by

$$\sigma_{\mathrm{R}}(x) = -\frac{2\sigma_0}{t} x, \quad -\frac{t}{2} \leq x \leq \frac{t}{2}, \tag{A.3}$$

where σ_0 is the maximum residual stress, which is on the surface of the ring. In this case, the resultant force and moment of the residual stress can be written as

$$F_{\mathrm{R}} = \int_A \sigma_{\mathrm{R}} dA = -\int_{-h/2}^{h/2} \int_{-t/2}^{t/2} \frac{2\sigma_0}{t} x dx dz = 0, \tag{A.4}$$

$$M_{\mathrm{R}} = \int_A \sigma_{\mathrm{R}} x dA = -\int_{-h/2}^{h/2} \int_{-t/2}^{t/2} \frac{2\sigma_0}{t} x^2 dx dz = -\frac{1}{6}\sigma_0 h t^2 = -\frac{1}{6} E \varepsilon_0 h t^2, \tag{A.5}$$

in which A is the cross-sectional area. By setting the two bending moments equal, i.e., $M_{\mathrm{T}} = M_{\mathrm{R}}$, we have

$$\varepsilon_0 = 1.5 \varepsilon_{\mathrm{T}}. \tag{A.6}$$

For a modified hexagonal ring with a specific natural state, the corresponding thermal strain in FEA simulations can be easily converted to the residual strain used in our rod model by using Eq. (A.6).

Appendix B. Governing equations and boundary conditions

B.1. Governing equations for the modified hexagonal ring

Governing equations for the jth ($j = 1, 2, 3, 4$) segment of the hexagonal ring are given by

$$\frac{d\bar{F}_1^{(j)}}{d\bar{s}^{(j)}} = \left(\bar{F}_2^{(j)} \bar{\kappa}_3^{(j)} - \bar{F}_3^{(j)} \bar{\kappa}_2^{(j)} \right) \ell^{(j)}, \tag{B.1}$$

$$\frac{d\bar{F}_2^{(j)}}{d\bar{s}^{(j)}} = \left(\bar{F}_3^{(j)} \bar{\kappa}_1^{(j)} - \bar{F}_1^{(j)} \bar{\kappa}_3^{(j)} \right) \ell^{(j)}, \tag{B.2}$$

$$\frac{d\bar{F}_3^{(j)}}{d\bar{s}^{(j)}} = \left(\bar{F}_1^{(j)} \bar{\kappa}_2^{(j)} - \bar{F}_2^{(j)} \bar{\kappa}_1^{(j)} \right) \ell^{(j)}, \tag{B.3}$$

$$\frac{d\bar{\kappa}_1^{(j)}}{d\bar{s}^{(j)}} = \frac{d\bar{\kappa}_{01}^{(j)}}{d\bar{s}} + \left[\beta \left(\bar{\kappa}_2^{(j)} - \bar{\kappa}_{02}^{(j)} \right) \bar{\kappa}_3^{(j)} - \left(\bar{\kappa}_3^{(j)} - \bar{\kappa}_{03}^{(j)} \right) \bar{\kappa}_2^{(j)} + \bar{F}_2^{(j)} \right] \frac{\ell^{(j)}}{\alpha}, \tag{B.4}$$

$$\frac{d\bar{\kappa}_2^{(j)}}{d\bar{s}^{(j)}} = \frac{d\bar{\kappa}_{02}^{(j)}}{d\bar{s}} - \left[\alpha \left(\bar{\kappa}_1^{(j)} - \bar{\kappa}_{01}^{(j)} \right) \bar{\kappa}_3^{(j)} - \left(\bar{\kappa}_3^{(j)} - \bar{\kappa}_{03}^{(j)} \right) \bar{\kappa}_1^{(j)} + \bar{M}_{\mathrm{R}} \bar{\kappa}_3^{(j)} + \bar{F}_1^{(j)} \right] \frac{\ell^{(j)}}{\beta}, \tag{B.5}$$

$$\frac{d\bar{\kappa}_3^{(j)}}{d\bar{s}^{(j)}} = \frac{d\bar{\kappa}_{03}^{(j)}}{d\bar{s}} + \left[\alpha\left(\bar{\kappa}_1^{(j)} - \bar{\kappa}_{01}^{(j)}\right)\bar{\kappa}_2^{(j)} - \beta\left(\bar{\kappa}_2^{(j)} - \bar{\kappa}_{02}^{(j)}\right)\bar{\kappa}_1^{(j)} + \bar{M}_R\bar{\kappa}_2^{(j)}\right]\ell^{(j)},\tag{B.6}$$

$$\frac{d\bar{r}_1^{(j)}}{d\bar{s}^{(j)}} = 2\left(q_1^{(j)}q_3^{(j)} + q_0^{(j)}q_2^{(j)}\right)\ell^{(j)},\tag{B.7}$$

$$\frac{d\bar{r}_2^{(j)}}{d\bar{s}^{(j)}} = 2\left(q_2^{(j)}q_3^{(j)} - q_0^{(j)}q_1^{(j)}\right)\ell^{(j)},\tag{B.8}$$

$$\frac{d\bar{r}_3^{(j)}}{d\bar{s}^{(j)}} = 2\left[\left(q_0^{(j)}\right)^2 + \left(q_3^{(j)}\right)^2 - \frac{1}{2}\right]\ell^{(j)},\tag{B.9}$$

$$\frac{dq_0^{(j)}}{d\bar{s}^{(j)}} = \frac{1}{2}\left(-q_1^{(j)}\bar{\kappa}_1^{(j)} - q_2^{(j)}\bar{\kappa}_2^{(j)} - q_3^{(j)}\bar{\kappa}_3^{(j)}\right)\ell^{(j)},\tag{B.10}$$

$$\frac{dq_1^{(j)}}{d\bar{s}^{(j)}} = \frac{1}{2}\left(q_0^{(j)}\bar{\kappa}_1^{(j)} - q_3^{(j)}\bar{\kappa}_2^{(j)} + q_0^{(j)}\bar{\kappa}_3^{(j)}\right)\ell^{(j)},\tag{B.11}$$

$$\frac{dq_2^{(j)}}{d\bar{s}^{(j)}} = \frac{1}{2}\left(q_3^{(j)}\bar{\kappa}_1^{(j)} + q_0^{(j)}\bar{\kappa}_2^{(j)} - q_1^{(j)}\bar{\kappa}_3^{(j)}\right)\ell^{(j)},\tag{B.12}$$

$$\frac{dq_3^{(j)}}{d\bar{s}^{(j)}} = \frac{1}{2}\left(-q_2^{(j)}\bar{\kappa}_1^{(j)} + q_1^{(j)}\bar{\kappa}_2^{(j)} + q_0^{(j)}\bar{\kappa}_3^{(j)}\right)\ell^{(j)},\tag{B.13}$$

in which

$$\alpha = \frac{EI_1}{GJ}, \beta = \frac{EI_2}{GJ}.\tag{B.14}$$

B.2. Boundary conditions for different loading methods

To obtain the boundary conditions for the modified hexagonal ring under different loading methods, the Euler angles are alternatively introduced to describe the transformation between the local basis (e_1, e_2, e_3) and the global basis (E_1, E_2, E_3), because this allows for more straightforward definition of the rotational boundary conditions. Here, the Euler angles (φ, θ, ϕ) following the rotation convention 3-2-3 are used (Healey and Mehta, 2005; Love, 2013; Yu and Hanna, 2019), which means that the local basis (starting with a frame aligned with the global basis) first rotates around e_3 by φ, then rotates around e_2 by θ, and finally rotates around e_3 by ϕ. Thus, we have

$$\begin{bmatrix} e_1 \\ e_2 \\ e_3 \end{bmatrix} = \begin{bmatrix} \cos\phi & \sin\phi & 0 \\ -\sin\phi & \cos\phi & 0 \\ 0 & 0 & 1 \end{bmatrix}\begin{bmatrix} \cos\theta & 0 & -\sin\theta \\ 0 & 1 & 0 \\ \sin\theta & 0 & \cos\theta \end{bmatrix}\begin{bmatrix} \cos\varphi & \sin\varphi & 0 \\ -\sin\varphi & \cos\varphi & 0 \\ 0 & 0 & 1 \end{bmatrix}\begin{bmatrix} E_1 \\ E_2 \\ E_3 \end{bmatrix}.\tag{B.15}$$

By setting the coefficient matrices of Eqs. (14) and (B.15) equal, the quaternion components (q_0, q_1, q_2, q_3) are expressed by the Euler angles (φ, θ, ϕ) as

$$q_0 = \cos\frac{\theta}{2}\cos\frac{\phi+\varphi}{2}, q_1 = \sin\frac{\theta}{2}\sin\frac{\phi-\varphi}{2}, q_2 = \sin\frac{\theta}{2}\cos\frac{\phi-\varphi}{2}, q_3 = \cos\frac{\theta}{2}\sin\frac{\phi+\varphi}{2}.\tag{B.16}$$

With the help of Eq. (B.16), the rotational boundary conditions defined by the Euler angles can be converted to those of quaternion components used in the Kirchhoff rod model.

As shown in Fig. B1, we take one quarter of the hexagonal ring for analyzes in theoretical modeling, and further divide the quarter ring into 4 segments. When the external loading is applied at the corners (Fig. B1(a)), the half straight edge at the bottom of the ring is taken as the first segment. When the external loading is applied at the edges (Fig. B1(b)), half of the rounded corner at the bottom of the ring is taken as the first segment. There are 52 governing equations for the hexagonal ring, which requires 52 boundary conditions to form a well-posed boundary value problem. Here, we directly give the 13 boundary conditions at the left boundary $\bar{s}^{(1)} = 0$ of the first segment and the right boundary $\bar{s}^{(4)} = 1$ of the fourth segment for different loading methods. The remaining 39 boundary conditions at the joints of neighboring segments can be easily obtained by considering the equilibrium and geometric compatibility. For the derivation details of boundary conditions for twisting load, refer to our previous work (Sun et al., 2022a). The boundary conditions for bending and point loads can be derived in a similar way. Once the governing equations are solved, the external loads required to prescribe the twisting angle Φ, the bending angle Θ, and the displacement δ can be obtained using the corresponding internal moment and force at the loading points, which equal $EI_2k_2^{(4)}$, $GJk_3^{(4)}$, and $F_2^{(4)}$, respectively.
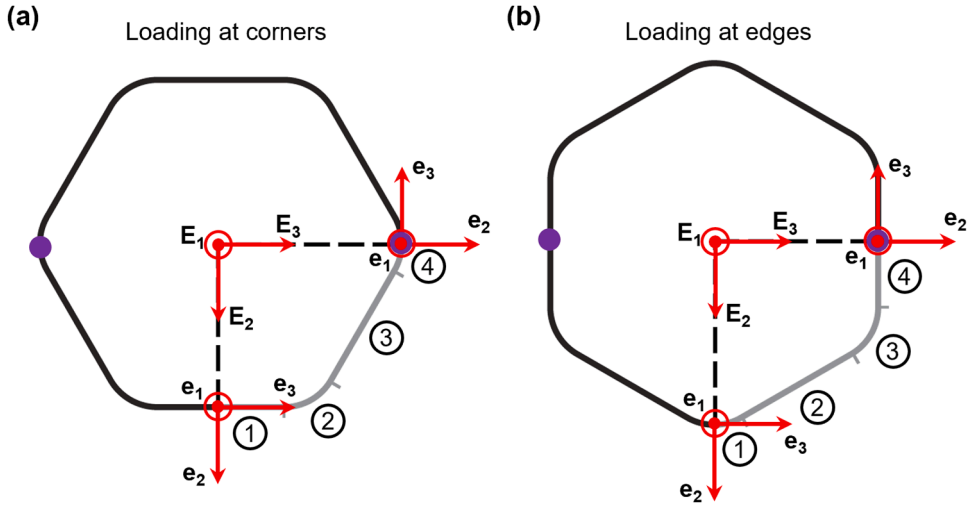
Fig. B1. Schematics of the hexagonal ring considered in the rod model. (a) External loading applied at the corners. (b) External loading applied at the edges. The global basis ($\mathbf{E}_1$, $\mathbf{E}_2$, $\mathbf{E}_3$) is fixed at the center of the ring, and the local basis ($\mathbf{e}_1$, $\mathbf{e}_2$, $\mathbf{e}_3$) is attached to the centerline of the ring's edge. The red dots represent the coordinate axis pointing out of the plane, the purple dots denote the loading points, and the circled numbers denote the segment number.

B.2.1. Twisting load

When the hexagonal ring is under twisting load, the boundary conditions at $\bar{s}^{(1)} = 0$ are written as

$$\bar{r}_1^{(1)}(0) = 0, \bar{r}_3^{(1)}(0) = 0, \bar{F}_2^{(1)}(0) = 0, \bar{\kappa}_2^{(1)}(0) = 0, q_1^{(1)}(0) = 0, q_3^{(1)}(0) = 0. \tag{B.17}$$

The boundary conditions at $\bar{s}^{(4)} = 1$ are given by

$$\bar{r}_1^{(4)}(1) = 0, \bar{r}_2^{(4)}(1) = 0, \bar{F}_2^{(4)}(1) = 0, q_0^{(4)}(1) = \frac{\sqrt{2}}{2}\cos\left(\frac{\Phi}{2}\right),$$

$$q_1^{(4)}(1) = \frac{\sqrt{2}}{2}\cos\left(\frac{\Phi}{2}\right), q_2^{(4)}(1) = -\frac{\sqrt{2}}{2}\sin\left(\frac{\Phi}{2}\right), q_3^{(4)}(1) = -\frac{\sqrt{2}}{2}\sin\left(\frac{\Phi}{2}\right). \tag{B.18}$$

B.2.2. Bending load

When the hexagonal ring is subjected to bending load, the boundary conditions at $\bar{s}^{(1)} = 0$ can be written as

$$\bar{r}_1^{(1)}(0) = 0, \bar{r}_3^{(1)}(0) = 0, \bar{F}_2^{(1)}(0) = 0, \bar{\kappa}_3^{(1)}(0) = 0, q_1^{(1)}(0) = 0, q_2^{(1)}(0) = 0. \tag{B.19}$$

The boundary conditions at $\bar{s}^{(4)} = 1$ are given by

$$\bar{F}_1^{(4)}(1) = 0, \bar{F}_2^{(4)}(1) = 0, \bar{r}_2^{(4)}(1) = 0, q_0^{(4)}(1) = \frac{\sqrt{2}}{2}\cos\left(\frac{\Theta}{2}\right),$$

$$q_1^{(4)}(1) = \frac{\sqrt{2}}{2}\cos\left(\frac{\Theta}{2}\right), q_2^{(4)}(1) = \frac{\sqrt{2}}{2}\sin\left(\frac{\Theta}{2}\right), q_3^{(4)}(1) = -\frac{\sqrt{2}}{2}\sin\left(\frac{\Theta}{2}\right). \tag{B.20}$$

B.2.3. Point load

For the case of point load, the boundary conditions at $\bar{s}^{(1)} = 0$ are written as

$$\bar{r}_1^{(1)}(0) = 0, \bar{r}_3^{(1)}(0) = 0, \bar{F}_2^{(1)}(0) = 0, \bar{\kappa}_2^{(1)}(0) = 0, q_1^{(1)}(0) = 0, q_3^{(1)}(0) = 0. \tag{B.21}$$

The boundary conditions at $\bar{s}^{(4)} = 1$ are given by

$$\bar{r}_1^{(4)}(1) = 0, \bar{r}_2^{(4)}(1) = 0, \bar{r}_3^{(4)}(1) = (c + r - \delta/2)\Big/a, \bar{\kappa}_2^{(4)}(1) = 0,$$

$$q_0^{(4)}(1) = q_1^{(4)}(1), q_2^{(4)}(1) = q_3^{(4)}(1), \left[q_0^{(4)}(1)\right]^2 + \left[q_2^{(4)}(1)\right]^2 = 1\Big/2. \tag{B.22}$$

Appendix C. Strain energy

In the present work, the residual strain is introduced into the ring as an internal moment, thus the strain energy in the Kirchhoff rod model with the consideration of the residual strain is given by

$$
\begin{aligned}
U_{\mathrm{rod}} &= \int_S \frac{(M_1 + M_{\mathrm{R}})^2}{2EI_1}ds + \int_S \frac{M_2^2}{2EI_2}ds + \int_S \frac{M_3^2}{2GJ}ds \\
&= \frac{1}{2}\left[\int_S EI_1(\kappa_1 - \kappa_{01})^2 ds + \int_S EI_2(\kappa_2 - \kappa_{02})^2 ds + \int_S GJ(\kappa_3 - \kappa_{03})^2 ds + \int_S 2M_{\mathrm{R}}(\kappa_1 - \kappa_{01})ds + \int_S \frac{M_{\mathrm{R}}^2}{EI_1}ds\right].
\end{aligned}
\tag{C.1}
$$

Note that the strain energy only includes the bending energy and the twisting energy without any stretching energy due to the inextensible assumption. By using Eq. (C.1), the normalized strain energy of the modified hexagonal ring can be written as

$$
\begin{aligned}
\bar{U} &= \frac{Ua}{GJ} = 2\sum_{i=1}^4 \left[\int_S \alpha\left(\bar{\kappa}_1^{(j)} - \bar{\kappa}_{01}^{(j)}\right)^2 \ell^{(j)} d\bar{s}^{(j)} + \int_S \beta\left(\bar{\kappa}_2^{(j)} - \bar{\kappa}_{02}^{(j)}\right)^2 \ell^{(j)} d\bar{s}^{(j)} \right. \\
&\quad \left. + \int_S \left(\bar{\kappa}_3^{(j)} - \bar{\kappa}_{03}^{(j)}\right)^2 \ell^{(j)} d\bar{s}^{(j)} + \int_S 2\bar{M}_{\mathrm{R}}\left(\bar{\kappa}_1^{(j)} - \bar{\kappa}_{01}^{(j)}\right)\ell^{(j)} d\bar{s}^{(j)} + \int_S \frac{\bar{M}_{\mathrm{R}}^2}{\alpha}\ell^{(j)} d\bar{s}^{(j)}\right].
\end{aligned}
\tag{C.2}
$$

With the help of Eq. (C.2), variation of the normalized strain energy with respect to the twisting angle of the modified hexagonal ring during the folding process can be obtained. We find that the theoretical results are in excellent agreement with the FEA results when the residual strain is not considered ($\varepsilon_0 = 0$). However, when incorporating the residual strain, the strain energy predicted by the rod model is always lower than the FEA results, but the two methods give the same trends for the energy landscapes. To identify this issue, we further compare the initial strain energy induced by the thermal strain and the residual strain. The initial strain energy of the bilayer ring considered in the FEA simulation is given by

$$U_1 = 2 \cdot \frac{1}{2}\int_V \sigma_{\mathrm{T}}\varepsilon_{\mathrm{T}}dV = \int_S \sigma_{\mathrm{T}}\varepsilon_{\mathrm{T}}h(t/2)ds = \frac{1}{2}\sigma_{\mathrm{T}}\varepsilon_{\mathrm{T}}htS_0, \tag{C.3}$$

where S_0 is the total length of the hexagonal ring. The initial strain energy of the single layer ring predicted by the rod model can be calculated as

$$U_2 = \int_S \frac{M_{\mathrm{R}}^2}{2EI_1}ds = \frac{M_R^2 S_0}{2EI_1} = \frac{3}{8}\sigma_{\mathrm{T}}\varepsilon_{\mathrm{T}}htS_0 \tag{C.4}$$

Based on Eqs. (C.3) and (C.4), we have

$$\Delta U = U_1 - U_2 = \frac{1}{8}\sigma_{\mathrm{T}}\varepsilon_{\mathrm{T}}htS_0 \tag{C.5}$$

As expected, the initial strain energy obtained by the rod model is lower than that of FEA simulations, which means although the thermal strain and the residual strain produce the same bending moment, the initial strain energy introduced into the ring are different. In Section 2.4, we modify the initial strain energy of the rod model by adding ΔU, and it is seen from Figs. 5(d) and 6(c) that the strain energy curves with residual strain evaluated by the rod model also agree with the FEA results very well.

Appendix D. Additional results for bending, twisting, and point loads

Additional results for folding behaviors of the modified hexagonal ring under bening, twisting, and point loads are given in Figs. D1, D2, D3, D4, D5, D6, D7, D8, and D9.
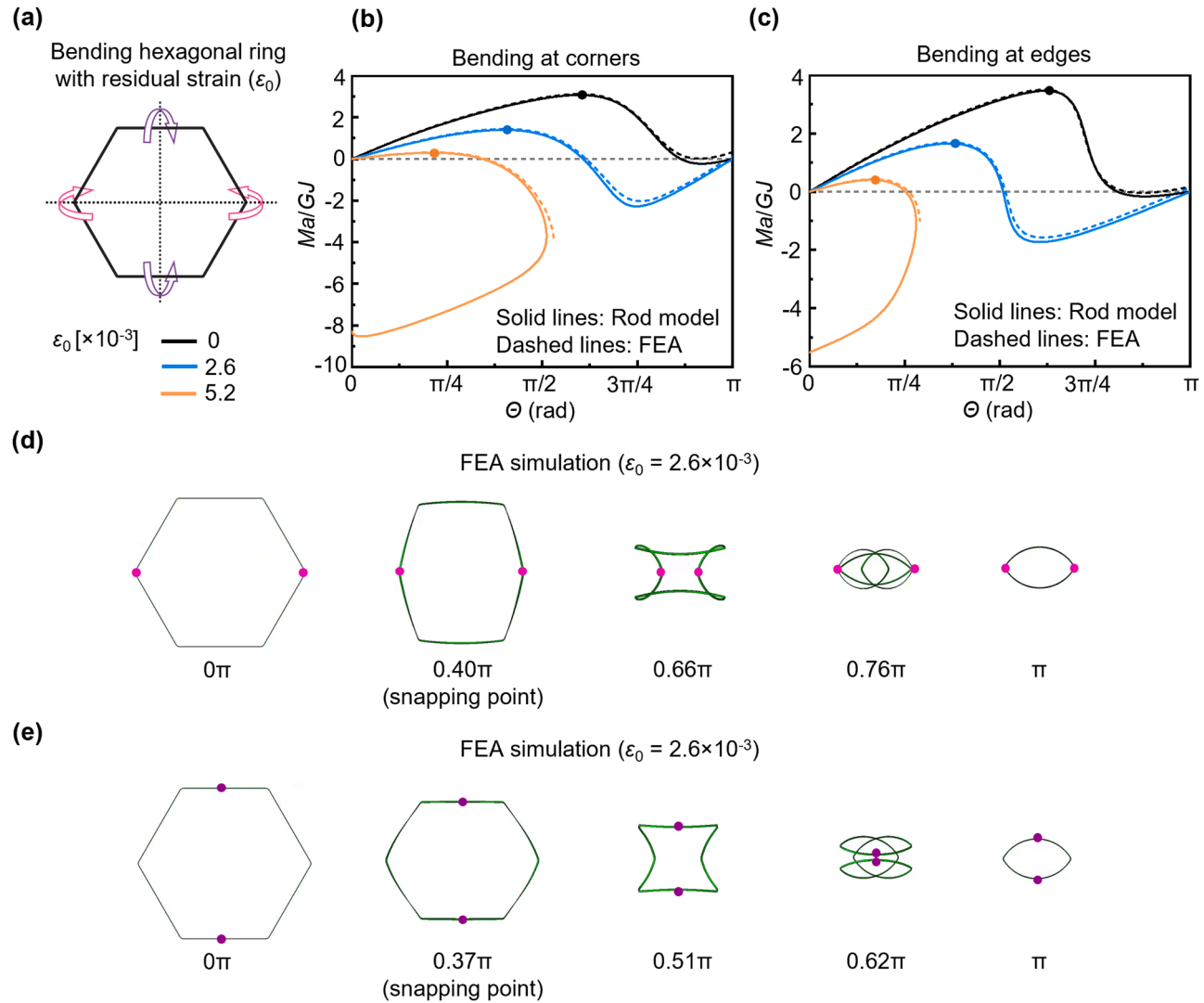
(a)

Bending hexagonal ring
with residual strain (ε_0)

ε_0 [×10^{-3}]
— 0
— 2.6
— 5.2

(b)

Bending at corners

Solid lines: Rod model
Dashed lines: FEA

Ma/GJ

Θ (rad)

(c)

Bending at edges

Solid lines: Rod model
Dashed lines: FEA

Ma/GJ

Θ (rad)

(d)

FEA simulation ($\varepsilon_0 = 2.6×10^{-3}$)

0π

0.40π
(snapping point)

0.66π

0.76π

π

(e)

FEA simulation ($\varepsilon_0 = 2.6×10^{-3}$)

0π

0.37π
(snapping point)

0.51π

0.62π

π

Fig. D1. Snap-folding of the modified hexagonal ring with residual strain under bending loads at different positions. (a) Schematic of the modified hexagonal ring under a pair of bending moments at corners or edges. (b,c) Normalized moment versus bending angle for the modified hexagonal ring with different residual strains under bending at corners (b) and at edges (c). (d,e) Folding processes of the modified hexagonal ring with residual strain $\varepsilon_0 = 0.0026$ under bending loads at corners (d) and at edges (e), with the dots denoting the loading points.
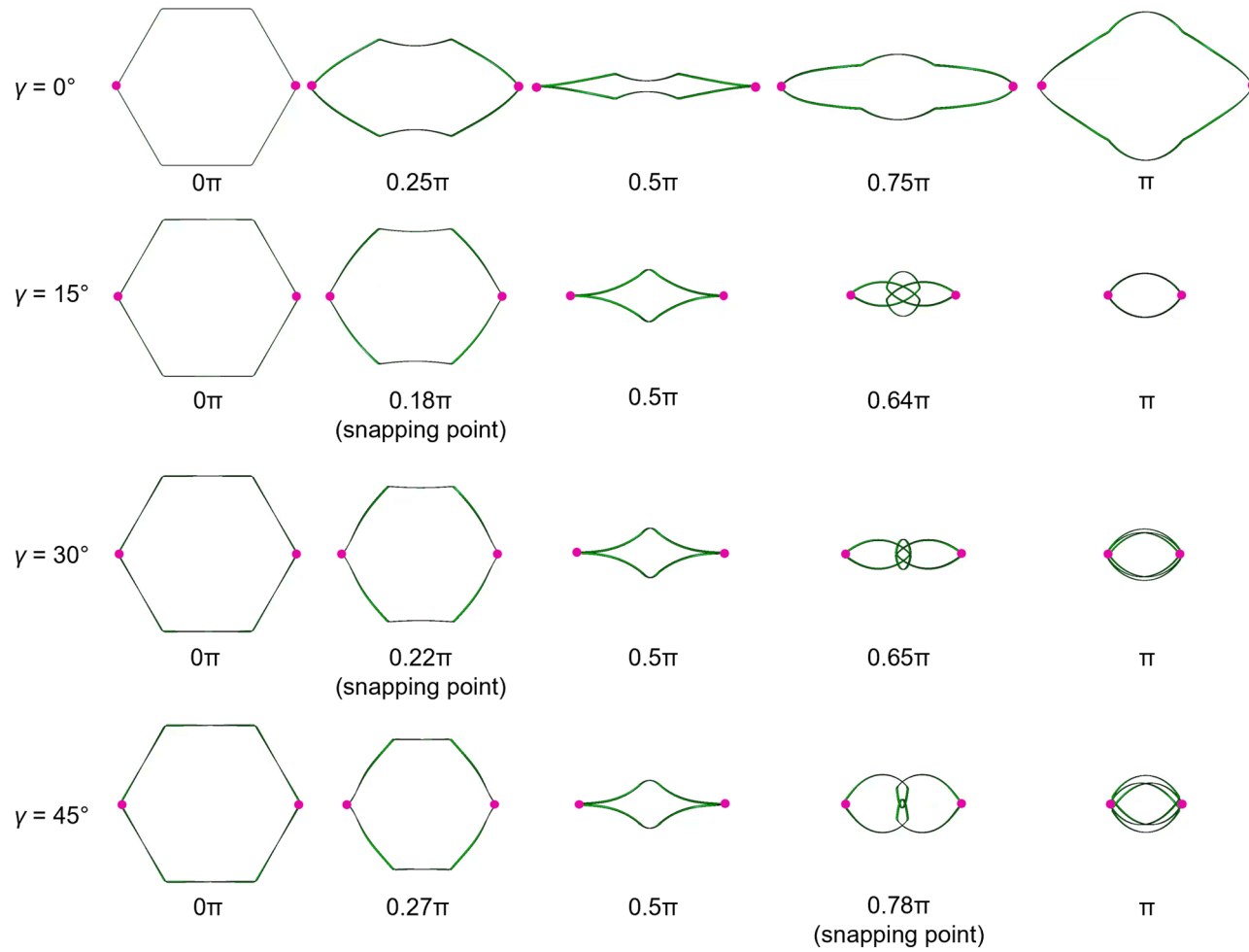
Fig. D2. Deformation configurations during folding processes of the modified hexagonal ring with different pre-twisted angles of the edges under negative twisting loads at corners. The dots correspond to the loading points.
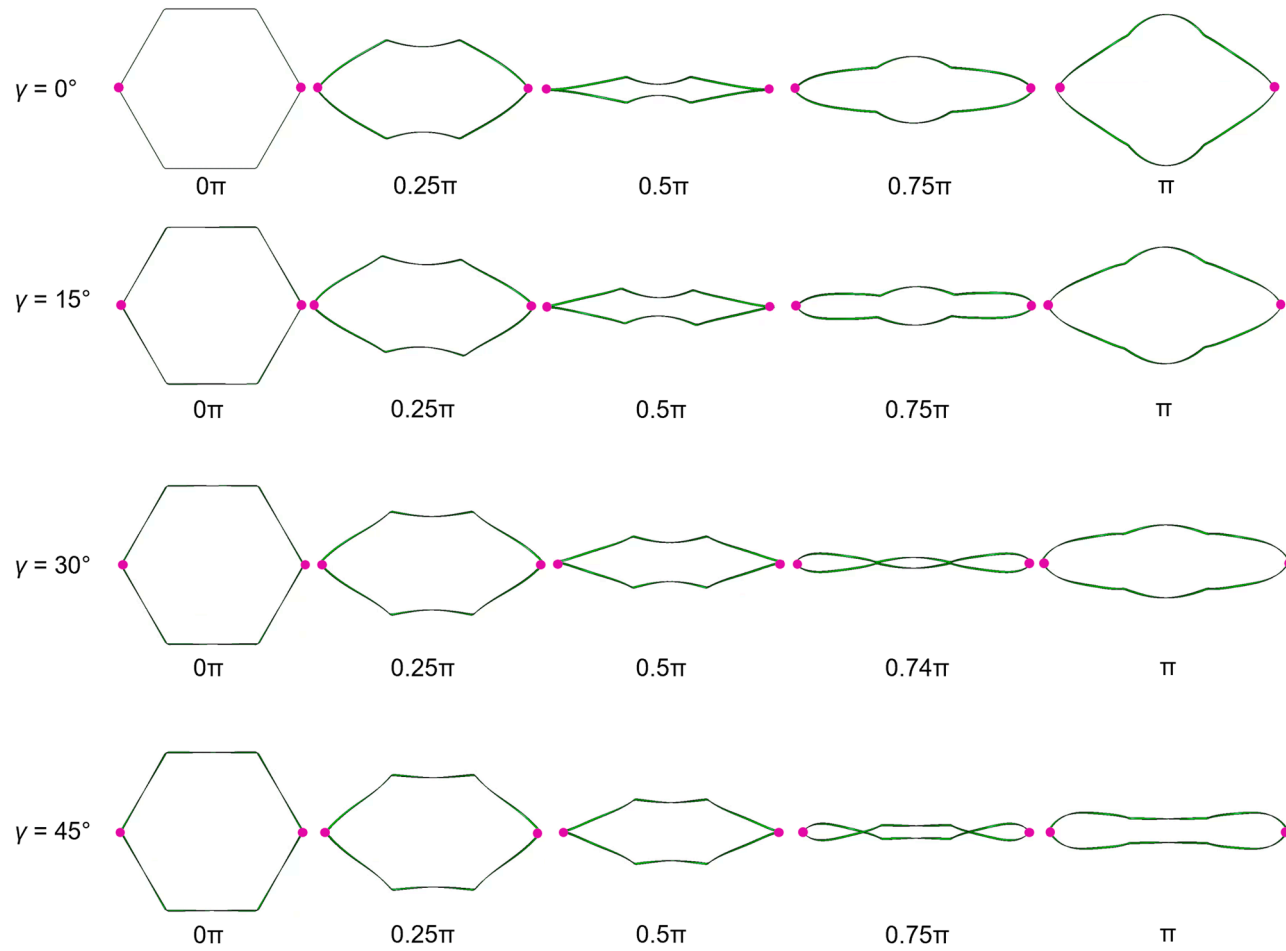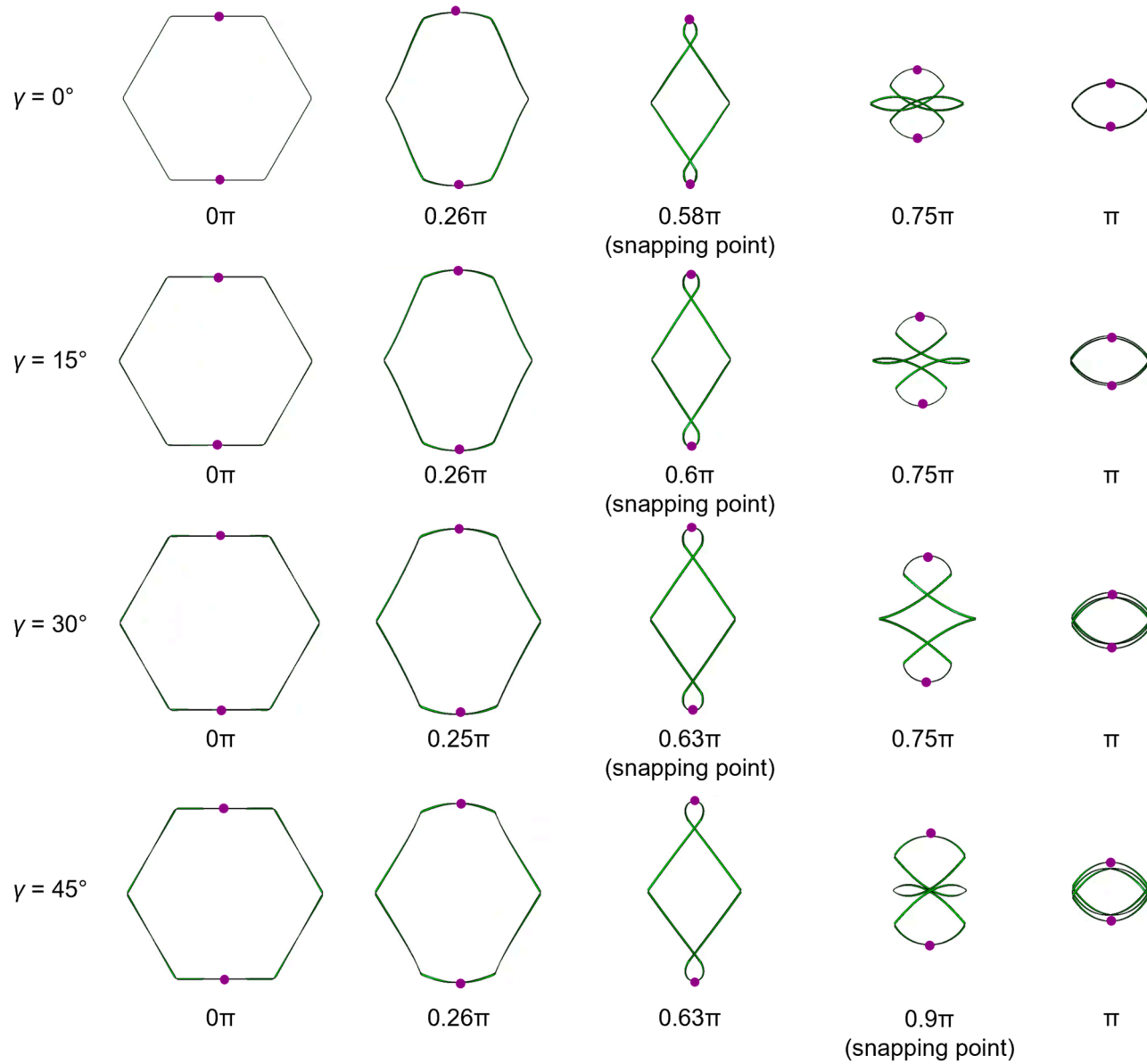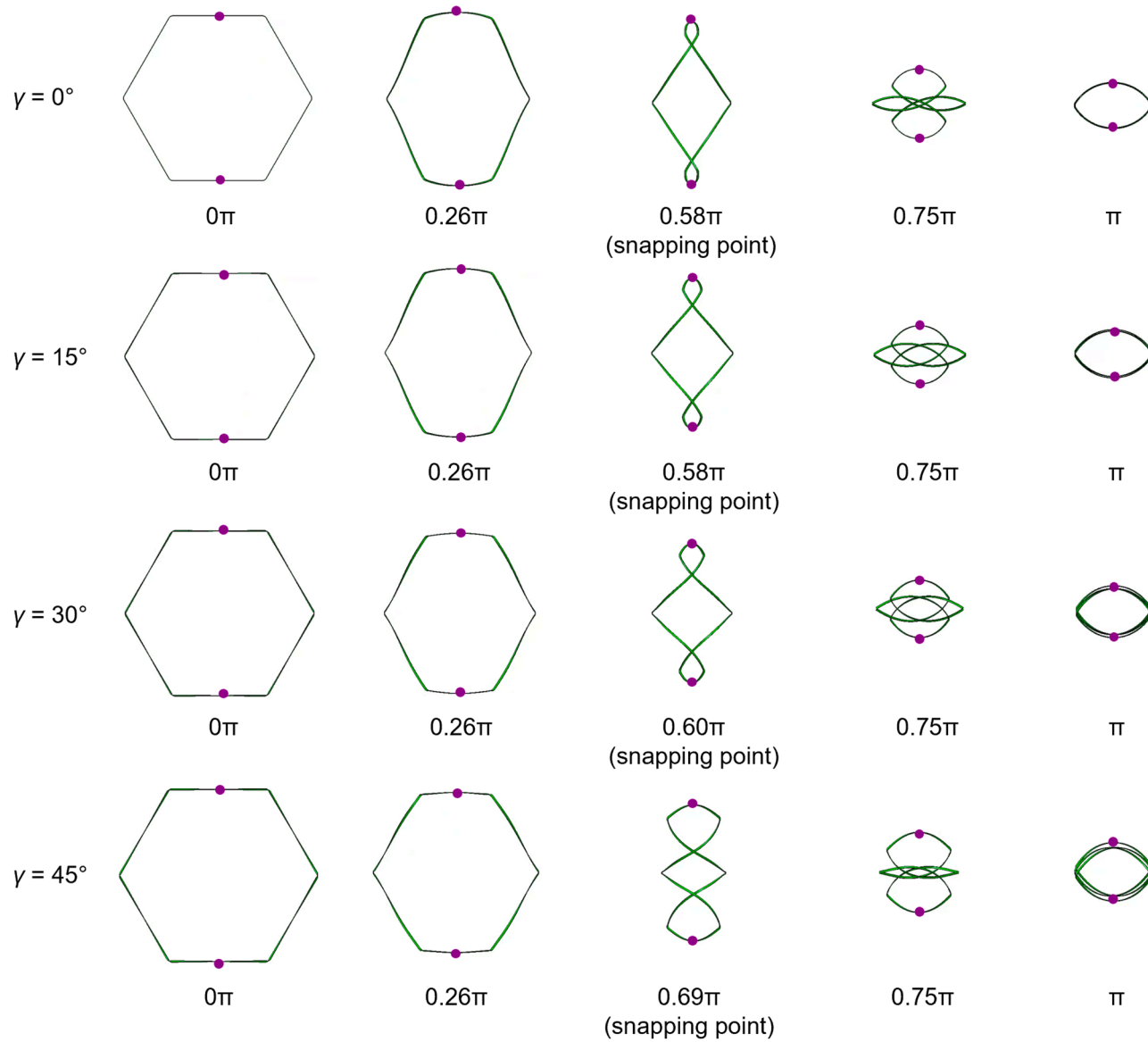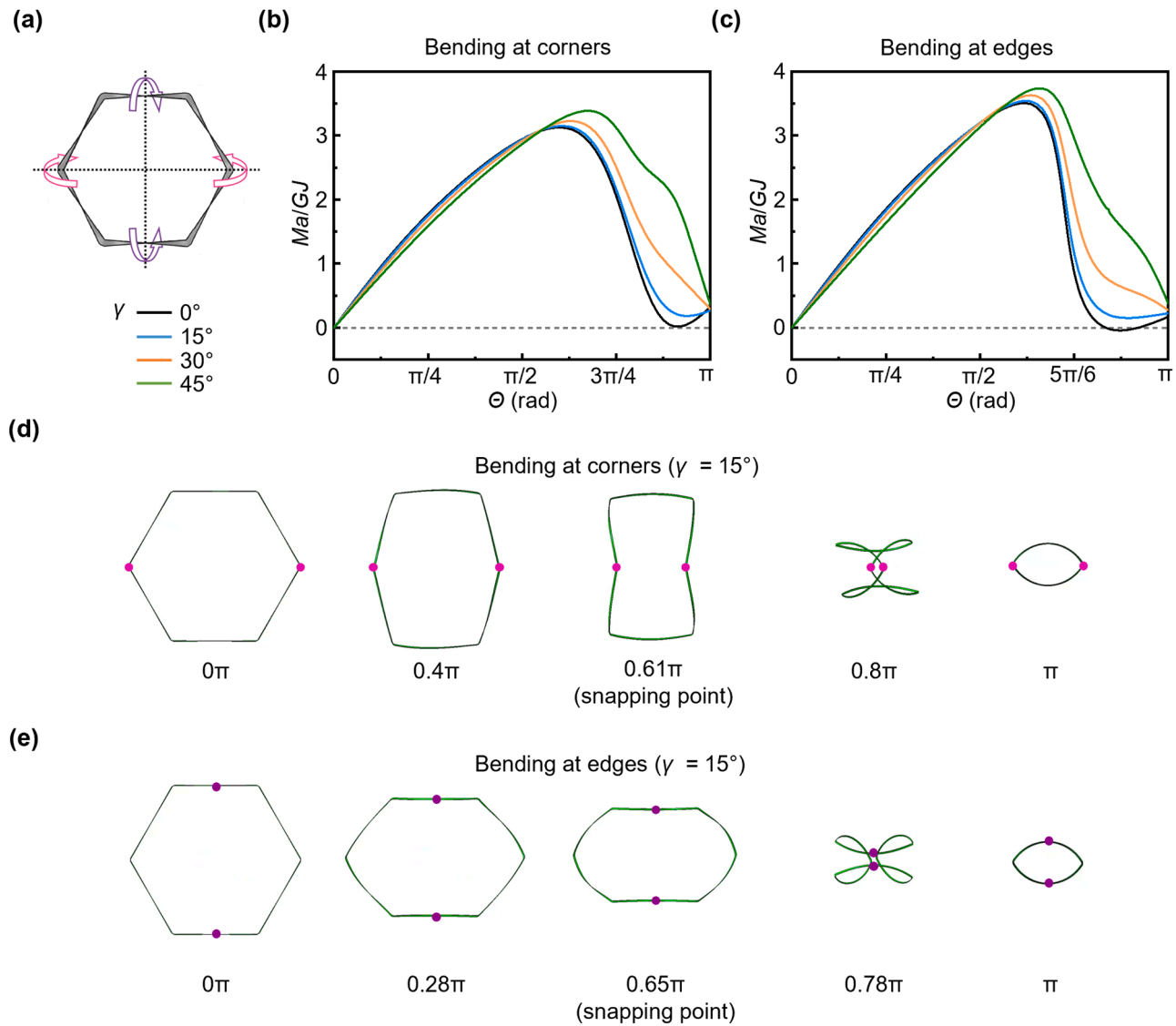
Fig. D3. Deformation configurations during folding processes of the modified hexagonal ring with different pre-twisted angles of the edges under positive twisting loads at corners. The dots correspond to the loading points.

Fig. D4. Folding processes of the modified hexagonal ring with different pre-twisted angles of the edges under negative twisting loads at edges. The dots correspond to the loading points.

Fig. D5. Folding processes of the modified hexagonal ring with different pre-twisted angles of the edges under positive twisting loads at edges. The dots correspond to the loading points.

Fig. D6. Snap-folding of the modified hexagonal ring with pre-twisted edges under bending loads at different positions predicted by FEA simulations. (a) Schematic of the modified hexagonal ring under a pair of bending moments at corners or edges. (b,c) Normalized moment versus bending angle for the modified hexagonal ring with different pre-twisted angles of the edges under bending loads at corners (b) and at edges (c). (d,e) Folding processes of the modified hexagonal ring with pre-twisted angle $\gamma = 15°$ of the edges under bending loads at corners (d) and at edges (e), with the dots denoting the loading points.
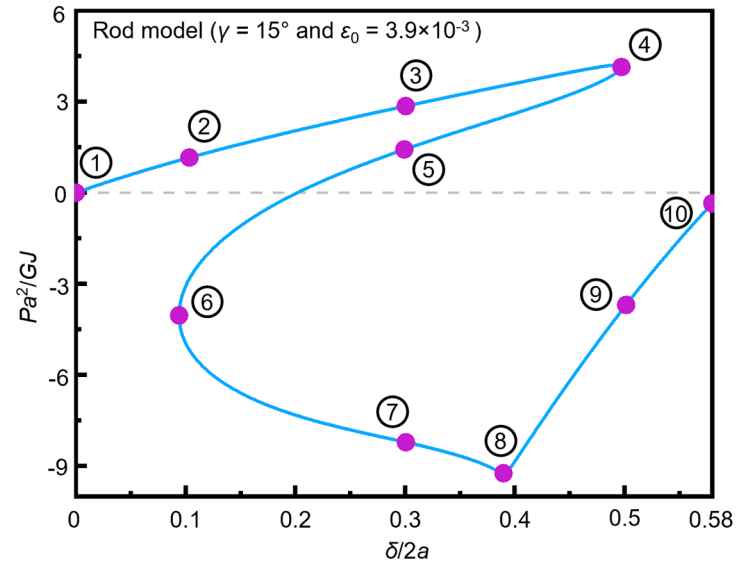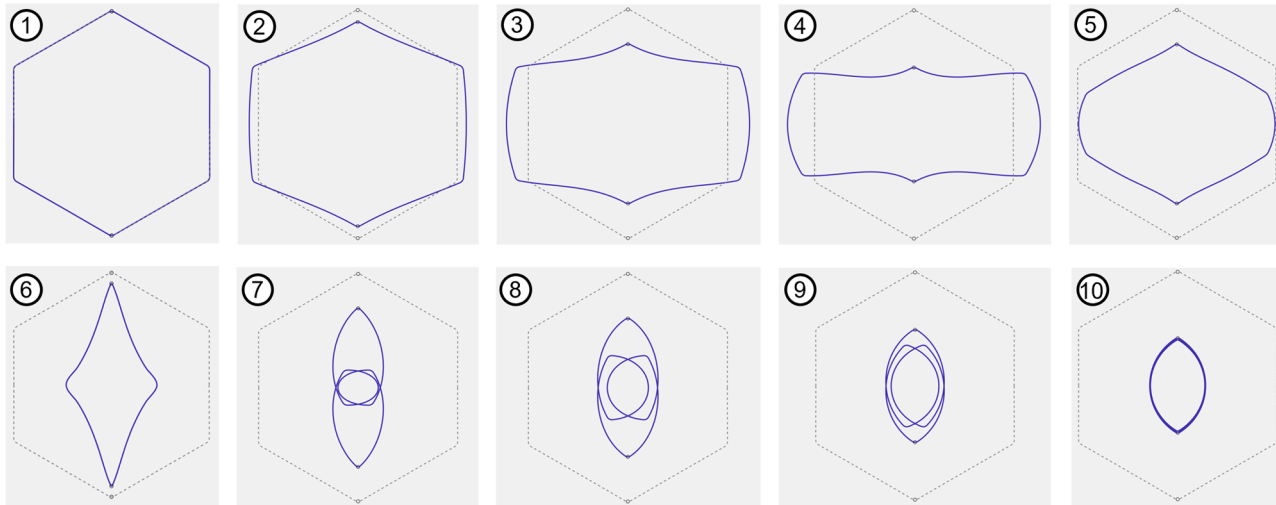
Fig. D7. Folding process of the modified hexagonal ring with residual strain $\varepsilon_0=0.0039$ and pre-twisted angle $\gamma = 15°$ of the edges under a point load predicted by the rod model.
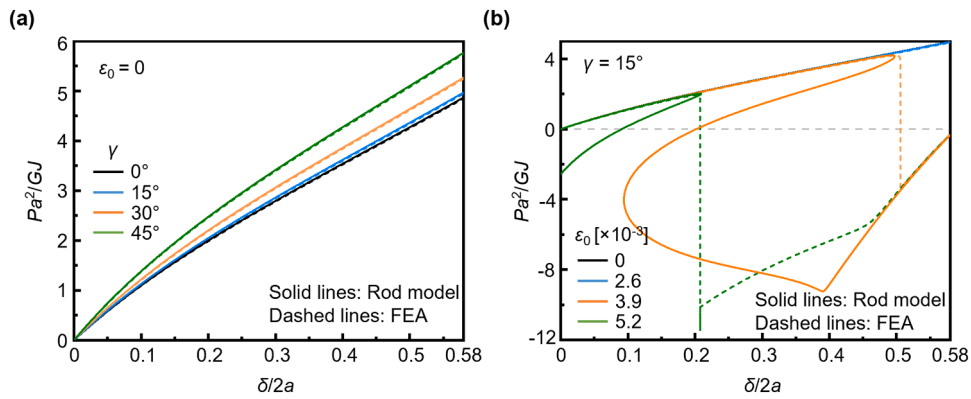
(a)

(b)

Fig. D8. Normalized force versus displacement for the modified hexagonal ring under a point load. (a) The modified hexagonal ring with only pre-twisted angles of the edges. (b) The modified hexagonal with residual strain and pre-twisted angle $\gamma = 15°$ of the edges.
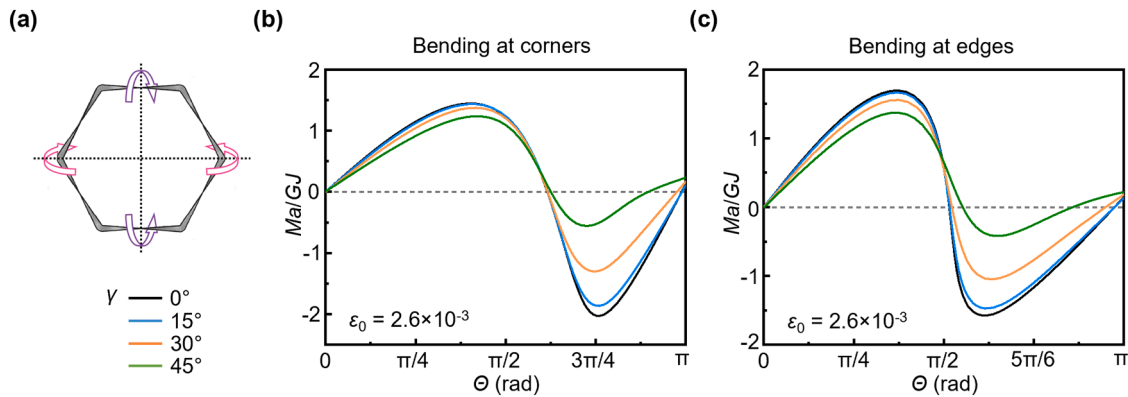
(a)

(b)

(c)

Fig. D9. Snap-folding of the modified hexagonal ring with residual strain and different pre-twisted angles of the edges under bending loads predicted by FEA simulations. (a) Schematic of the modified hexagonal ring under a pair of bending moments at corners or edges. (b,c) Normalized moment versus twisting angle for bending loads applied at corners (b) and at edges (c).

References

Audoly, B., Neukirch, S., 2021. A one-dimensional model for elastic ribbons: a little stretching makes a big difference. J. Mech. Phys. Solids 153, 104457.

Audoly, B., Pomeau, Y., 2010. Elasticity and Geometry: From Hair Curls to the Non-Linear Response of Shells. Oxford University Press.

Bae, J., Na, J.H., Santangelo, C.D., Hayward, R.C., 2014. Edge-defined metric buckling of temperature-responsive hydrogel ribbons and rings. Polymer 55, 5908–5914.

Barreto, D.D., Saxena, S., Kumar, A., 2022. A magnetoelastic theory for Kirchhoff rods having uniformly distributed paramagnetic inclusions and its buckling. Int. J. Solids Struct. 234, 111147.

Cadogan, D., Stein, J., Grahne, M., 1999. Inflatable composite habitat structures for lunar and mars exploration. Acta Astronaut. 44, 399–406.

Celli, P., Lamaro, A., McMahan, C., Bordeenithikasem, P., Hofmann, D., Daraio, C., 2020. Compliant morphing structures from twisted bulk metallic glass ribbons. J. Mech. Phys. Solids 145, 104129.

Chen, M., Goyal, R., Majji, M., Skelton, R.E., 2021. Review of space habitat designs for long term space explorations. Prog. Aerosp. Sci. 122, 100692.

Chen, T., Bilal, O.R., Lang, R., Daraio, C., Shea, K., 2019. Autonomous deployment of a solar panel using elastic origami and distributed shape-memory-polymer actuators. Phys. Rev. Appl. 11, 064069.

Chopin, J., Kudrolli, A., 2013. Helicoids, wrinkles, and loops in twisted ribbons. Phys. Rev. Lett. 111, 174302.

Coleman, B.D., Swigon, D., 2004. Theory of self–contact in Kirchhoff rods with applications to supercoiling of knotted and unknotted DNA plasmids. Philos. Trans. R. Soc. Lond. Ser. A Math. Phys. Eng. Sci. 362, 1281–1299.

Dankowicz, H., Schilder, F., 2011. An extended continuation problem for bifurcation analysis in the presence of constraints. J. Comput. Nonlinear Dyn. 6 (3), 031003.

Dankowicz, H., Schilder, F., 2013. Recipes for Continuation. SIAM.

Dias, M.A., Audoly, B., 2014. A non-linear rod model for folded elastic strips. J. Mech. Phys. Solids 62, 57–80.

Dias, M.A., Dudte, L.H., Mahadevan, L., Santangelo, C.D., 2012. Geometric mechanics of curved crease origami. Phys. Rev. Lett. 109, 114301.

Dill, E.H., 1992. Kirchhoff's theory of rods. Arch. Hist. Exact Sci. 1–23.

Dinh, H.P., Démery, V., Davidovitch, B., Brau, F., Damman, P., 2016. From cylindrical to stretching ridges and wrinkles in twisted ribbons. Phys. Rev. Lett. 117, 104301.

Domokos, G., Healey, T., 2001. Hidden symmetry of global solutions in twisted elastic rings. J. Nonlinear Sci. 11, 47–67.

Filipov, E.T., Tachi, T., Paulino, G.H., 2015. Origami tubes assembled into stiff, yet reconfigurable structures and metamaterials. Proc. Natl Acad. Sci. 112, 12321–12326.

Fu, H., Nan, K., Bai, W., Huang, W., Bai, K., Lu, L., Zhou, C., Liu, Y., Liu, F., Wang, J., 2018. Morphable 3D mesostructures and microelectronic devices by multistable buckling mechanics. Nat. Mater. 17, 268–276.

Gan, W.W., Pellegrino, S., 2006. Numerical approach to the kinematic analysis of deployable structures forming a closed loop. Proc. Inst. Mech. Eng. Part C J. Mech. Eng. Sci. 220, 1045–1056.

Gomez, M., Moulton, D.E., Vella, D., 2017. Critical slowing down in purely elastic 'snap-through'instabilities. Nat. Phys. 13, 142–145.

Goriely, A., 2006. Twisted elastic rings and the rediscoveries of Michell's instability. J. Elast. 84, 281–299.

Grandgeorge, P., Sano, T.G., Reis, P.M., 2022. An elastic rod in frictional contact with a rigid cylinder. J. Mech. Phys. Solids 164, 104885.

Han, B., Xu, Y., Yao, J., Zheng, D., Li, Y., Zhao, Y., 2019. Design and analysis of a scissors double-ring truss deployable mechanism for space antennas. Aerosp. Sci. Technol. 93, 105357.

Healey, T.J., Mehta, P., 2005. Straightforward computation of spatial equilibria of geometrically exact cosserat rods. Int. J. Bifurc. Chaos 15, 949–965.

Huang, W., Wang, Y., Li, X., Jawed, M.K., 2020. Shear induced supercritical pitchfork bifurcation of pre-buckled bands, from narrow strips to wide plates. J. Mech. Phys. Solids 145, 104168.

Hutchinson, J.W., 2020. Instabilities of embedded cylindrical inclusions undergoing isotropic swelling or growth. Extrem. Mech. Lett. 40, 100879.

Ishida, S., Nojima, T., Hagiwara, I., 2015. Regular folding pattern for deployable nonaxisymmetric tubes. J. Mech. Des. 137, 091402.

Kaczmarski, B., Moulton, D.E., Kuhl, E., Goriely, A., 2022. Active filaments I: Curvature and torsion generation. J. Mech. Phys. Solids 164, 104918.

Korte, A., Starostin, E., Van Der Heijden, G., 2011. Triangular buckling patterns of twisted inextensible strips. Proc. R. Soc. A Math. Phys. Eng. Sci. 467, 285–303.

Kuribayashi, K., Tsuchiya, K., You, Z., Tomus, D., Umemoto, M., Ito, T., Sasaki, M., 2006. Self-deployable origami stent grafts as a biomedical application of Ni-rich TiNi shape memory alloy foil. Mater. Sci. Eng. A 419, 131–137.

Leanza, S., Wu, S., Dai, J., Zhao, R.R., 2022. Hexagonal ring origami assemblies? Foldable functional structures with extreme packing. J. Appl. Mech. 89 (8), 081003.

Lessinnes, T., Moulton, D.E., Goriely, A., 2017. Morphoelastic rods part II: growing birods. J. Mech. Phys. Solids 100, 147–196.

Liu, M., Gomez, M., Vella, D., 2021. Delayed bifurcation in elastic snap-through instabilities. J. Mech. Phys. Solids 151, 104386.

Love, A.E.H., 2013. A Treatise on the Mathematical Theory of Elasticity. Cambridge University Press.

Luan, H., Zhang, Q., Liu, T.L., Wang, X., Zhao, S., Wang, H., Yao, S., Xue, Y., Kwak, J.W., Bai, W., 2021. Complex 3D microfluidic architectures formed by mechanically guided compressive buckling. Sci. Adv. 7, eabj3686.

Manning, R.S., Maddocks, J.H., 1999. Symmetry breaking and the twisted elastic ring. Comput. Method Appl. Mech. Eng. 170, 313–330.

Melancon, D., Gorissen, B., García-Mora, C.J., Hoberman, C., Bertoldi, K., 2021. Multistable inflatable origami structures at the metre scale. Nature 592, 545–550.

Miller, J.T., Lazarus, A., Audoly, B., Reis, P.M., 2014. Shapes of a suspended curly hair. Phys. Rev. Lett. 112, 068103.

Moulton, D., Lessinnes, T., Goriely, A., 2013. Morphoelastic rods. Part I: a single growing elastic rod. J. Mech. Phys. Solids 61, 398–427.

Moulton, D.E., Lessinnes, T., Goriely, A., 2020. Morphoelastic rods III: differential growth and curvature generation in elastic filaments. J. Mech. Phys. Solids 142, 104022.

Mouthuy, P.O., Coulombier, M., Pardoen, T., Raskin, J.P., Jonas, A.M., 2012. Overcurvature describes the buckling and folding of rings from curved origami to foldable tents. Nat. Commun. 3, 1–8.

Neukirch, S., Van Der Heijden, G., Thompson, J., 2002. Writhing instabilities of twisted rods: from infinite to finite length. J. Mech. Phys. Solids 50, 1175–1191.

Patil, V.P., Sandt, J.D., Kolle, M., Dunkel, J., 2020. Topological mechanics of knots and tangles. Science 367, 71–75.

Peng, X., Wu, S., Sun, X., Yue, L., Montgomery, S.M., Demoly, F., Zhou, K., Zhao, R.R., Qi, H.J., 2022. 4D printing of freestanding liquid crystal elastomers via hybrid additive manufacturing. Adv. Mater., 2204890

Qiu, L., Hutchinson, J.W., Amir, A., 2022. Bending instability of rod-shaped bacteria. Phys. Rev. Lett. 128, 058101.

Roach, D.J., Sun, X., Peng, X., Demoly, F., Zhou, K., Qi, H.J., 2022. 4D printed multifunctional composites with cooling-rate mediated tunable shape morphing. Adv. Funct. Mater., 2203236

Sano, T.G., Pezzulla, M., Reis, P.M., 2022. A Kirchhoff-like theory for hard magnetic rods under geometrically nonlinear deformation in three dimensions. J. Mech. Phys. Solids 160, 104739.

Sano, T.G., Wada, H., 2019. Twist-induced snapping in a bent elastic rod and ribbon. Phys. Rev. Lett. 122, 114301.

Santiago-Prowald, J., Baier, H., 2013. Advances in deployable structures and surfaces for large apertures in space. CEAS Sp. J. 5, 89–115.

Sharma, H., Upadhyay, S., 2022. Deployable toroidal structures based on modified Kresling pattern. Mech. Mach. Theory 176, 104972.

Starostin, E., Van Der Heijden, G., 2007. The shape of a Möbius strip. Nat. Mater. 6, 563–567.

Sun, X., Wu, S., Dai, J., Leanza, S., Yue, L., Yu, L., Jin, Y., Qi, H.J., Zhao, R.R., 2022a. Phase diagram and mechanics of snap-folding of ring origami by twisting. Int. J. Solids Struct. 248, 111685.

Sun, X., Yue, L., Yu, L., Shao, H., Peng, X., Zhou, K., Demoly, F., Zhao, R., Qi, H.J., 2022b. Machine learning-evolutionary algorithm enabled design for 4d-printed active composite structures. Adv. Funct. Mater. 32, 2109805.

Timoshenko, S., Goodier, J.N., 1951. Theory of Elasticity: by S. Timoshenko and JN Goodier. McGraw-Hill.

Wu, S., Dai, J., Leanza, S., Zhao, R.R., 2022. Hexagonal ring origami—Snap-folding with large packing ratio. Extrem. Mech. Lett. 53, 101713.

Wu, S., Yue, L., Jin, Y., Sun, X., Zemelka, C., Qi, H.J., Zhao, R., 2021. Ring origami: snap-folding of rings with different geometries. Adv. Intell. Syst. 3, 2100107.

Yan, Z., Wang, K., Wang, B., 2022. Buckling of circular rings and its applications in thin-film electronics. Int. J. Mech. Sci. 228, 107477.

Yoshiaki, G., Yasuhito, W., Toshihiro, K., Makoto, O., 1992. Elastic buckling phenomenon applicable to deployable rings. Int. J. Solids Struct. 29, 893–909.

You, Z., Pellegrino, S., 1997. Cable-stiffened pantographic deployable structures part 2: mesh reflector. AIAA J. 35, 1348–1355.

Yu, T., Dreier, L., Marmo, F., Gabriele, S., Parascho, S., Adriaenssens, S., 2021. Numerical modeling of static equilibria and bifurcations in bigons and bigon rings. J. Mech. Phys. Solids 152, 104459.

Yu, T., Hanna, J., 2019. Bifurcations of buckled, clamped anisotropic rods and thin bands under lateral end translations. J. Mech. Phys. Solids 122, 657–685.

Ze, Q., Kuang, X., Wu, S., Wong, J., Montgomery, S.M., Zhang, R., Kovitz, J.M., Yang, F., Qi, H.J., Zhao, R., 2020. Magnetic shape memory polymers with integrated multifunctional shape manipulation. Adv. Mater. 32, 1906657.

Zhang, F., Li, S., Shen, Z., Cheng, X., Xue, Z., Zhang, H., Song, H., Bai, K., Yan, D., Wang, H., 2021. Rapidly deployable and morphable 3D mesostructures with applications in multimodal biomedical devices. Proc. Natl Acad. Sci. 118, e2026414118.

Zhao, S., Gu, L., Froemming, S.R., 2012. Performance of self-expanding Nitinol stent in a curved artery: impact of stent length and deployment orientation. J. Biomech. Eng. 134.

Zirbel, S.A., Lang, R.J., Thomson, M.W., Sigel, D.A., Walkemeyer, P.E., Trease, B.P., Magleby, S.P., Howell, L.L., 2013. Accommodating thickness in origami-based deployable arrays. J. Mech. Des. 135.